

Broadband Decoupling of Intensity and Polarization with Vectorial Fourier Metasurfaces

Qinghua Song

Université Côte d'Azur, <https://orcid.org/0000-0002-4622-0418>

Arthur Baroni

Aix-Marseille University <https://orcid.org/0000-0003-4294-7158>

Pin Chieh Wu

National Cheng Kung University <https://orcid.org/0000-0002-5781-9696>

Sébastien Chenot

Centre de Recherche sur l'Hétéro-Epitaxie et ses Applications

Virginie Brandli

Centre de Recherche sur l'Hétéro-Epitaxie et ses Applications

Stephane Vezean

French National Centre for Scientific Research <https://orcid.org/0000-0002-4521-047X>

Benjamin Damilano

Centre de Recherche sur l'Hétéro-Epitaxie et ses Applications

Philippe Mierry

Centre de Recherche sur l'Hétéro-Epitaxie et ses Applications

Samira Khadir

Centre de Recherche sur l'Hétéro-Epitaxie et ses Applications

Patrick Ferrand

Aix-Marseille University <https://orcid.org/0000-0002-7395-5663>

Patrice Genevet (✉ pg@crhea.cnrs.fr)

French National Centre for Scientific Research

Article

Keywords: intensity, polarization, vectorial fourier metasurfaces

Posted Date: January 12th, 2021

DOI: <https://doi.org/10.21203/rs.3.rs-140769/v1>

License:   This work is licensed under a Creative Commons Attribution 4.0 International License.

[Read Full License](#)

Version of Record: A version of this preprint was published at Nature Communications on June 15th, 2021. See the published version at <https://doi.org/10.1038/s41467-021-23908-0>.

1 **Broadband Decoupling of Intensity and Polarization with**
2 **Vectorial Fourier Metasurfaces**

3

4 Qinghua Song¹, Arthur Baroni², Pin Chieh Wu³, Sébastien Chenot¹, Virginie Brandli¹,
5 Stéphane Vézian¹, Benjamin Damilano¹, Philippe de Mierry¹, Samira Khadir¹, Patrick
6 Ferrand² and Patrice Genevet^{1*}

7

8 ¹ *Université Cote d'Azur, CNRS, CRHEA, Rue Bernard Gregory, Sophia Antipolis 06560*
9 *Valbonne, France*

10 ² *Aix Marseille univ, CNRS, Centrale Marseille, Institut Fresnel, 13013 Marseille,*
11 *France*

12 ³ *Department of Photonics, National Cheng Kung University, Tainan 70101, Taiwan*

13

14 * *Corresponding Author: Patrice.Genevet@crhea.cnrs.fr*

15 **ABSTRACT**

16 **Intensity and polarization are two fundamental components of light. Independently**
17 **control of them is of tremendous interest in many applications. In this paper, we**
18 **propose a general vectorial encryption method, which enables arbitrary far-field light**
19 **distribution with the local polarization, including orientations and ellipticities,**
20 **decoupling intensity from polarization across a broad bandwidth using geometric**
21 **phase metasurfaces. By revamping the well-known iterative Fourier transform**
22 **algorithm, we propose “à la carte” design of far-field intensity and polarization**
23 **distribution with vectorial Fourier metasurfaces. A series of non-conventional**
24 **vectorial field distribution, mimicking cylindrical vector beams in the sense that they**
25 **share the same intensity profile but with different polarization distribution and a**
26 **speckled phase distribution, is demonstrated. Vectorial Fourier optical metasurfaces**
27 **may enable important applications in the area of complex light beam generation,**
28 **secure optical data storage, steganography and optical communications.**

29 **Introduction**

30 Optical waveform control plays a critical role in the optical systems for various applications.
31 Among the different methods to address the electromagnetic field distribution in the far-
32 field, optical metasurfaces¹⁻¹², artificial materials that consist of subwavelength structure
33 arrays, are capable of tailoring the waveform of the electromagnetic waves with
34 unprecedented level of precision. In particular, due to the versatility of this approach, it is
35 possible to engineer both amplitude and polarization information at will. Vectorial meta-
36 holograms with arbitrary polarization have been developed using diatomic reflective
37 metasurface^{13,14} and geometric phase based metasurface¹⁵. However, the generated
38 polarization is limited by the multiplexing metasurface's sub-pixels, which yet are not able
39 to realize arbitrary spatially distributed polarization. Some efforts have been made by
40 combining geometric phase and propagation phase^{16,17}, but it severely suffers from narrow
41 bandwidth. A broadband wavefront control that can decouple amplitude from polarization
42 information has yet to be demonstrated.

43 One of the most important applications of meta-holograms is information security, which
44 is important in many areas of the society, such as protecting individuals, industries and
45 military information from leaks and stealing. Among the different communication channels
46 and information sharing techniques, photonics is the most efficient and effective way of
47 carrying information across long distances. Optical waveforms possess many degrees of
48 freedom, such as amplitude, phase, frequency and polarization, and each can be used for
49 data encoding. Moreover, optical encoding methods require specific professional
50 equipment for data encoding, providing a more secure way towards high security
51 information encoding. Various optical encoding methods have been developed based on

52 the intensity, such as spatial correlators¹⁸, optical XOR image encryption¹⁹, phase shifting
53 interferometry²⁰, polarization dependent images^{21,22}, Lippmann plate²³ and holograms^{24,25}.
54 Many other efforts of optical encoding have been made by using multiplexing meta-
55 hologram that can encode the optical information into multi-channels of holographic
56 images²⁶⁻³². The most common approach is based on polarization-dependent meta-
57 hologram, which creates different holographic images using different polarizations of the
58 incident beam³³⁻³⁷. Chiral meta-holograms are also introduced for direction-dependent
59 holographic encoding³⁸⁻⁴⁰. Other encoding methods relying on incident wavelength⁴¹,
60 nonlinear effect⁴², spatial frequency⁴³, orbital angular momentum^{44,45} and tunable
61 metasurface^{46,47} are also demonstrated. Note that all of these proposed multiplexing meta-
62 holograms encode information on the intensity of the holographic images.

63 In this paper, we propose a vectorial Fourier metasurface for which amplitude and
64 polarization information can be addressed independently one from the other. We utilize
65 this specificity to encode intensity and two polarization information channels, namely
66 ellipticity and azimuth, to produce far-field decoupled images. The image refers to the
67 spatially distribution of either total intensity, ellipticity or azimuth information. The design
68 of the metasurface is realized using a modified iterative Fourier transform (IFT) algorithm
69 that does not only consider far-field amplitude but also the far-field polarization spatial
70 distribution. Our calculation results consist of discretized transmission matrices
71 representing the spatial amplitude and polarization into pixelated profiles. The design of
72 the nanostructured interfaces capable of matching these distributions requires therefore
73 precise control of all properties of transmitted light. To this end, we composed arbitrary

74 amplitude, phase and polarization pixels by superposing two amplitude-modulated and
75 phase-delayed beams with opposite circular polarizations (CP).

76 With respect to previously proposed methods, our approach defines the metasurface
77 capability by considering the polarization distribution in the far field only, i.e., as a result
78 of the propagation leading to LCP and RCP far-fields. Since the metasurface plane is
79 encoded via the Fourier transformation of targeted fields, the realization of optical
80 information encoding in this work is completely outperforming than that of previous
81 demonstrations with multiplexing¹⁵. As a proof of principle, we designed a series of far-
82 field intensity profiles presenting a given donut-like intensity distribution structured with
83 different polarization orientations. Interestingly, these vectorial fields look-alike the well-
84 known cylindrical vector beams (CVB, previously discussed in the literature). They differ
85 nevertheless strongly to CVB in the sense that, even if the polarization is maintained, their
86 long range far-field phase distribution is lost during the optimization process. Roughly
87 speaking, the randomization of the far-field phase using IFT techniques produces granular
88 intensity distributions, or intensity-modulated speckle signals, that match the overall
89 targeted CVB donut intensity and polarization. These field profiles are extremely
90 interesting, as they are mixing long range transverse coherence with very short range
91 spatial phase correlation. In addition, we demonstrate a class of optical interfaces that
92 encodes the orientation angle and ellipticity angle of the polarization in a uniformly
93 distributed intensity profile. In order to resolve the encoded information, we use both
94 conventional Stokes parameter measurements and vectorial ptychography to characterize
95 both metasurface and their far-field complex amplitudes.

96

97 **Results**

98 **Design Method.** The design principle of the vectorial Fourier metasurface is shown in
 99 Figure 1. Each pixel of the metasurface consists of four lines of phase gradient supercells
 100 as shown in Figure 1a, in which the top two lines and bottom two lines of meta-structures
 101 are arranged counter clockwise and clockwise, respectively, with the same orientation
 102 increment angle of δ_d . Each building block of the pixels, the pillar meta-structure, acts as
 103 half-waveplate that converts the handedness of the incident CP beams and imposes a
 104 geometry phase (also called Pancharatnam–Berry (PB) phase) of $\pm 2\delta$, where δ is the
 105 orientation angle of each pillar (the signs $-$ and $+$, denoted clockwise and counter
 106 clockwise rotation, respectively), i.e., $|+\rangle \rightarrow e^{i2\delta}|-\rangle$ and $|-\rangle \rightarrow e^{-i2\delta}|+\rangle$, where $|+\rangle$
 107 represents left circular polarization (LCP) and $|-\rangle$ represents right circular polarization
 108 (RCP). Considering that the incident linear polarized (LP) light can be decomposed into
 109 LCP and RCP, the clockwise lines in a pixel deflect the LCP light to RCP light with a
 110 deflection angle of $\theta_t = \arcsin\left(\frac{2\delta_d}{k_0 P}\right)$ as shown in Figure 1b, where k_0 is the wavenumber
 111 in the free space and P is the period of the unit-cell. While the counter clockwise lines in
 112 the same pixel deflect the RCP to LCP at the same angle of θ_t . The starting orientation
 113 angle (SOA) of the four lines from top to bottom are δ_+ , $\delta_+ + \Delta\delta_+$, δ_- , and $\delta_- + \Delta\delta_-$,
 114 where $\Delta\delta_{\pm}$ and δ_{\pm} are respectively used to control the relative amplitude and phase
 115 between LCP and RCP. We ignore the co-polarization in the following text simply because
 116 it is diffracted at the zero order, and it does not interfere with the cross polarized fields.
 117 The complex amplitude a^m in the metasurface plane is given by,

118
$$a^m(x^m, y^m) = A_+^m(x^m, y^m)e^{i\varphi_+^m(x^m, y^m)} + A_-^m(x^m, y^m)e^{i\varphi_-^m(x^m, y^m)} \quad (1)$$

119 where the superscript m represents the metasurface plane, x^m and y^m represent the pixels
120 position in the metasurface plane, $A_{\pm}^m(x^m, y^m)$ and $\varphi_{\pm}^m(x^m, y^m)$ are the amplitude and
121 phase of pixel (x^m, y^m) at the metasurface plane generated by the two CP of the light beam.
122 For simplicity, in the following we ignore the notation of (x^m, y^m) . The amplitude A_{\pm}^m is
123 controlled by the rotation angle difference of $\Delta\delta_{\pm}$ due to the interference between two lines
124 of LCP (or RCP) as,

$$125 \quad A_{\sigma}^m = |e^{-i2\sigma\delta_{\sigma}} + e^{-i2\sigma(\delta_{\sigma}+\Delta\delta_{\sigma})}|/2 = \sqrt{(1 + \cos 2\Delta\delta_{\sigma})}/2 \quad (2)$$

126 where $\sigma = +$ (or $+1$) represents LCP, $\sigma = -$ (or -1) represents RCP. The phase φ_{\pm}^m is
127 generated by the rotation angle of δ_{\pm} thanks to the geometric phase as,

$$128 \quad \varphi_{\sigma}^m = -2\sigma\delta_{\sigma} \quad (3)$$

129 Therefore, by varying the value of δ_{\pm} and $\Delta\delta_{\pm}$, arbitrary amplitude and phase information
130 in the metasurface plane can be assigned to each pixel independently from the others, so as
131 to control far-field amplitude and polarization information at will.

132 To decouple amplitude from far-field polarization information, we propose modifying the
133 conventional Gerchberg–Saxton (GS) algorithm to a version working for vectorial fields.
134 The GS utilizes iterative Fourier transform as shown in Figure 2 (see more details in
135 Supplementary Note 1)^{26,27,17}, and in its vectorial version, instead of converging to a phase
136 profile in the metasurface plane, we consider the phase profiles of two CP beams noted φ_{σ}^m
137 realized by rotating the angle of δ_{σ} according to Eq. 3. In this implementation, the far-field
138 polarization can be controlled over the entire profile, despite the fact that GS converges to
139 designs with randomly distributed far-field phase profile. The condition for far-field
140 polarization addressing requires that the phase retardation between orthogonal polarization

141 channels is properly adjusted, i.e., the phase value for both polarization channels is
 142 randomly distributed on the transverse plane with a controllable phase retardation.
 143 For a convenience purpose, we keep the amplitude in the metasurface plane A_{\pm}^m uniform
 144 for all pixels, i.e., $\Delta\delta_+$ and $\Delta\delta_-$ are two constant values for all pixels determined by the
 145 total intensity of two CP beams I_{\pm}^m . The latter are calculated considering the intensity
 146 integral of all pixels in the image plane as: $I_{\pm}^m = I_{\pm}^f = \sum_{x,y=1}^{N_x, N_y} (a_{\pm}^f(x^f, y^f))^2$, where the
 147 superscript f represents the far field image plane, (x^f, y^f) represent the pixel position in
 148 the far field image plane, $N_x \times N_y$ is the total pixel number, $a_{\pm}^f(x^f, y^f)$ are the amplitude
 149 of LCP and RCP light of each pixel (x^f, y^f) . It can be shown that the rotation angles $\Delta\delta_{\pm}$
 150 are given by (see more details in Supplementary Note 2),

$$151 \quad \begin{cases} \Delta\delta_{\sigma} = 0, & \text{if } I_{\sigma}^f \geq I_{-\sigma}^f \\ \Delta\delta_{\sigma} = \arccos\left(\frac{2 \sum_{x,y=1}^{N_x, N_y} (a_{\sigma}^f(x^f, y^f))^2}{\sum_{x,y=1}^{N_x, N_y} (a_{-\sigma}^f(x^f, y^f))^2} - 1\right) / 2, & \text{if } I_{\sigma}^f < I_{-\sigma}^f \end{cases} \quad (4)$$

152 Eq. 3 and 4 are then used to recover the orientation angles of each pixel of the metasurface.
 153 The meta-structures are simulated using full-wave finite-difference time-domain (FDTD)
 154 and the simulation results are shown in Figure 3. The top view and perspective view of one
 155 meta-structure are shown in Figure 3a and 3b, respectively. 1 μm -tall GaN nano-pillars,
 156 grown on low index lattice matched Sapphire substrate, are realized with rectangular cross
 157 sections to induce structural birefringence. Both GaN and sapphire are transparent in the
 158 entire visible range, which are perfect candidates for the design of visible optical
 159 metasurfaces. The period of the nanostructure unit-cell is $P = 300$ nm to avoid spurious
 160 diffraction effects in the substrate. The width is fixed to $L_v = 120$ nm. The circular
 161 polarization conversion efficiency is shown in Figure 3c with the long axis of the nanopillar

162 L_u swept from 160 nm to 260 nm and the wavelength λ swept from 450 nm to 700 nm. The
163 dash line indicates the CP conversion at $L_u = 210$ nm, where the CP conversion efficiency
164 is higher than 50% across almost the entire visible range. Figure 3d and 3e show the electric
165 field distribution along short and long axis of the pillar, respectively, at the point of $L_v =$
166 120 nm and $\lambda = 575$ nm (the purple star in Figure 3c). It is shown that there are 5.5 and 5
167 oscillations of electric field in E_x and E_y in the GaN nanopillar, i.e. a signature of half a
168 wavelength retardation difference, which verifies that the meta-structure acts as a
169 nanoscale half-waveplate for these structural parameters and operation wavelength.
170 Additionally, when the nanopillar is rotated with an angle of δ , a geometric phase of 2δ is
171 obtained on cross-circular polarization as shown in Fig 3f. The simulated geometric phase
172 by using FDTD shown in blue stars agrees well with the theoretical one ($\varphi_{RL} = 2\delta$) shown
173 by the red curve. In addition, the CP conversion efficiency between LCP and RCP is, as
174 expected, near unity as shown by the black curve.

175 In order to validate our approach to decouple intensity from polarization, we conceived a
176 series of spatially variant far-field polarization profiles distributed on a donut far-field
177 intensity profile (with the same radius), but having different azimuthal angle of the linear
178 polarization defined by $\psi(x, y) = l\varphi(x, y) + m\pi/2$, where l is an integer number that
179 represents the turns of the polarization rotation encircling the donut intensity profile, x and
180 y are the coordinate of beam, $\varphi(x, y) = \tan^{-1}(\frac{y}{x})$, $m = 0$ represents the radial mode and m
181 $= 1$ represents the azimuthal mode. We demonstrated four designs with different
182 combinations of m and l (see more details in Supplementary Figure S3). The scanning
183 electron microscope (SEM) images of the fabricated vectorial beam metasurfaces are
184 shown in the first row of Figure 4. The second row represents the designed intensity and

185 polarization profiles. The measured total intensity profiles are shown in the third row,
186 which agree well to the designed intensities. By placing a linear polarizer with different
187 rotation angles in front of the vectorial beams, different patterns are observed from the
188 fourth to the seventh rows. Interestingly even if these beams resembling to the well-known
189 cylindrical vector (CV) beams, we prove that they do not feature long-range spatial phase
190 correlation. To do so, we realized full Jones Matrix characterization of the metasurface
191 using vectorial ptychographic measurements based on the acquisition of series of
192 diffraction intensity patterns recorded by illuminating the metasurface at several
193 overlapping positions, to extract the far field complex amplitude distributions on crossed
194 polarization channels as shown in Figure 5, indicating short spatial phase correlation while
195 maintaining a long range polarization distribution. Indeed, with respect to CV beams that
196 are vectorial solutions of Maxwell's equations obeying axial symmetry in both amplitude
197 and phase, our solution to produce spatially distributed amplitude and polarization field
198 does not impose long range spatial phase correlation. These fields could be beneficial for
199 practical applications in laser machining, remote sensing, and so forth^{48,49} or to decouple
200 phase and polarization in singular optics. Using PB phase tuning mechanisms, the
201 polarization encoding is simply given by the rotation angle of the nanostructures, resulting
202 in a broad operating bandwidth. It reveals that broad operating bandwidth is generally not
203 achievable with a combination of propagation and PB phases¹⁶. The efficiency of the
204 hologram is around 15%, since the pixel size of the meta-hologram is larger than the
205 operating wavelength, so that higher order images generated, which decrease the efficiency
206 of the interested order. The characterization of the broadband properties is shown in Figure
207 6. A CV beam with $l = -2$ and $m = 0$ is measured from $\lambda = 475$ nm to $\lambda = 675$ nm. A donut

208 intensity profile is shown in the first row without polarizer. Subsequently, we insert a linear
 209 polarizer in front of the image. The same pattern is observed for all of the wavelength with
 210 fixed transmission axis of polarizer as shown from the second to fifth rows, indicating that
 211 the metasurface could maintain polarization distribution properties over a broad
 212 wavelength range.

213 After verification of the design approach with simple vectorial beam, we propose to encode
 214 optical information relying on the azimuth and ellipticity angles of the polarization
 215 information rather than encoding intensity profiles of conventional polarization states,
 216 realizing a sort of holographic polarization-only encoding technique. Two meta-holograms
 217 with the same intensity profile but different azimuth and ellipticity angles of the
 218 polarization are designed as shown in the Supplementary Figure S4. The fabricated results
 219 of the two metasurfaces are shown in Supplementary Figure S5. As the information is only
 220 encoded on the polarization properties, i.e. spatial distribution of the orientation and
 221 ellipticity, an additional retrieval method based on local Stokes polarimetry is required^{50,51}.
 222 Stokes parameters, which include the optical quantities of interest, are generally obtained
 223 using two sets of measurements, cascading a waveplate with the phase difference between
 224 fast axis and slow axis of ϕ , and a linear polarizer with rotation angle of θ with respect to
 225 the x -axis in front of the image. The measured intensity profiles after the cascaded
 226 waveplate and linear polarizer are related to ϕ and θ , which are denoted as $I(\theta, \phi)$.
 227 Therefore, the measured azimuth and ellipticity angles of the polarization are described as
 228 (see more details in Supplementary Note 3),

$$229 \quad \psi = \frac{1}{2} \tan^{-1} \left(\frac{2I(45^\circ, 0^\circ) - I(0^\circ, 0^\circ) - I(90^\circ, 0^\circ)}{I(0^\circ, 0^\circ) - I(90^\circ, 0^\circ)} \right) \quad \left(-\frac{\pi}{2} < \psi \leq \frac{\pi}{2} \right) \quad (5)$$

$$230 \quad \chi = \frac{1}{2} \sin^{-1} \left(\frac{I(0^\circ, 0^\circ) + I(90^\circ, 0^\circ) - 2I(45^\circ, 90^\circ)}{I(0^\circ, 0^\circ) + I(90^\circ, 0^\circ)} \right) \quad \left(-\frac{\pi}{4} < \chi \leq \frac{\pi}{4} \right) \quad (6)$$

231 Additional to these measurements, the total intensity profiles, i.e. with spatially varying
232 polarization distribution, are measured directly, without any wave plate and/or polarizer.
233 The measured results of the first metasurface are shown in Figure 7a-7c. As expected from
234 the design, a uniform intensity profile is observed in Figure 7a. However, both a “Blade”
235 and a “Rocket” images are shown when looking at the polarization spatial distribution in
236 the azimuth and ellipticity angles, respectively. Another design with the same uniform
237 intensity profile but a “Tree” and a “Squirrel” polarization information is obtained in Figure
238 7d-7f. Besides, we also used vectorial ptychography to map both the amplitude and
239 polarization information of the vectorial far field patterns (see more details in Methods and
240 Supplementary Figure S2b). It can retrieve the Jones matrix map of the metasurface as
241 shown in Supplementary Figure S6. By applying this Jones matrix to a linear polarization
242 incidence, one can reproduce all of the far-field information, such as intensity as shown in
243 Figure S7a and S7d, and polarization as shown in Figure S7b-S7c and S7e-S7f. As
244 expected, a uniformly distributed intensity profile is observed in both design of Figure S7a
245 and S7d. However, in the azimuth angle and ellipticity angle of polarization map, images
246 of “Blade” and “Rocket” are respectively obtained in Figure S7b and S7c, and images of
247 “Tree” and “Squirrel” are observed in Figure S7e and S7f.

248

249 **Discussion**

250 In conclusion, we have demonstrated a general method to design vectorial Fourier
251 metasurfaces which decouple intensity from polarization information, such that spatially
252 distributed full polarization profiles with arbitrary intensity distribution can be realized.
253 The vectorial Fourier metasurfaces are conceived using a modified iterative Fourier

254 transform algorithm that optimizes the transmission information properties to encode
255 simultaneously both intensity and polarization far-field distribution. We produce an
256 interesting series of far-field beam profile with donut-like intensity and spatially distributed
257 polarization, resembling cylindrical vector beams, but with randomly distributed far-field
258 phase distribution. To fully characterize the optical response of our Fourier-metasurfaces,
259 we retrieve the complete Jones matrix of the metasurface using ptychography and proved
260 that the short range phase correlation in contrast to the long range polarization distribution,
261 indicating that both polarization channels have spatially correlated phase profiles.
262 Furthermore, the proposed vectorial Fourier metasurfaces are able to encode complex
263 polarization information onto uniform distributed intensity profiles. We demonstrated that
264 a “Blade” (or “Tree”) and a “Rocket” (or “Squirrel”) images can be multiplexed and
265 separately decrypted from the orientation angle and ellipticity angle of the polarization on
266 a uniformly distributed intensity profile of a holographic image. Vectorial Fourier encoding
267 could highly enhance the information security, having various promising applications in
268 data encryption, optical ID tags for authentication and verification, high-density optical
269 data storage, but also for specific applications including optical trapping and laser
270 machining.

271 **Methods**

272 **Device fabrication**

273 A GaN thin-film with 1 μm thickness is grown on a double-side polished c-plane sapphire
274 substrate using molecular beam epitaxy (MBE) RIBER system. Conventional electron
275 beam lithography (EBL) processes are used for the etching of GaN nanopillars. The
276 PMMA resist (495A4) with ~ 180 nm is spin coated on the GaN and baked on a hot plate
277 with temperature of 125°C . It is exposed with designed patterns at 20 keV (Raith ElphyPlus,
278 Zeiss Supra 40) and developed in 3:1 IPA:MIBK solution. Oxygen plasma etching (RIE,
279 Oxford system) is used to clean the residual resist that is not completely removed during
280 development. The sample is deposited with a 50 nm thickness of Nickel using E-beam
281 evaporation and is immersed into acetone solution for lift-off process to obtain the Nickel
282 hard mask. By using reactive ion etching (RIE, Oxford system) with a plasma composed
283 of $\text{Cl}_2\text{CH}_4\text{Ar}$ gases, the pattern is transferred to the GaN. The residual nickel hard mask is
284 removed by chemical etching with 1:1 $\text{H}_2\text{O}_2\text{:H}_2\text{SO}_4$ solution, revealing the GaN nanopillars.

285

286 **Conventional optical setup**

287 The optical setup for characterizing the projected far-field is shown in Supplementary
288 Figure S2a. A laser beam propagates through a linear polarizer (WP25M-VIS) with axis of
289 transmission in horizontal direction to generate linear polarized input beam. After an
290 achromatic lens with a focal length of 50 mm, the laser beam is weakly focused on the
291 metasurfaces. The first-order holographic image is projected onto a projector placed 10 cm
292 away from the metasurface. A selected quarter waveplate with fast axis at the horizontal

293 and a linear polarizer with axis of transmission at angle θ are used to analyze the images
294 and measure the Stokes parameters.

295

296 **Optical vectorial ptychography**

297 A custom setup is used for the ptychography characterization⁵²⁻⁵⁴ as shown in
298 Supplementary Figure S2b. The metasurface is placed on a motorized stage (U-780, Physik
299 Instrumente) and scanned under a finite sized probe with effective diameter of 50 μm ,
300 selected optically by placing a 2-mm diameter iris diaphragm in the image plane of a 40 \times
301 objective lens (ACHN-P, NA 0.65, Olympus). The camera (Stingray F-145B, Allied Vision,
302 320 \times 240 effective pixels of 25.8 \times 25.8 μm^2 after binning) was placed 190 mm after the
303 diaphragm. Object reconstructions were performed by means of the conjugate gradient
304 algorithm running on a multi-graphics-processor-unit (DGX Station, NVIDIA), allowing
305 the estimation of Jones matrices of the meta-holograms. The vectorial exit field is given by
306 the matrix product of the previous calculated Jones matrices and a Jones vector of LP
307 illumination. The vectorial far field is further obtained by computing the far-field
308 propagation by fast Fourier transform of the exit field, allowing to quantify the complex
309 amplitude of the far field, including intensity, phase and polarization properties.

310 **Acknowledgement**

311 We acknowledge funding from the European Research Council (ERC) under the European
312 Union's Horizon 2020 research and innovation programme (Grant agreements no. 639109).
313 P.F. acknowledges funding from the European Research Council (ERC) under the
314 European Union's Horizon 2020 research and innovation programme (Grant agreement no.
315 724881). P.C.W. acknowledges the support from Ministry of Science and Technology,
316 Taiwan (Grant numbers: 108-2112-M-006-021-MY3; 107-2923-M-006-004-MY3) and
317 the support from Ministry of Education (Yushan Young Scholar Program), Taiwan. P.C.W.
318 also acknowledges the support in part by Higher Education Sprout Project, Ministry of
319 Education to the Headquarters of University Advancement at National Cheng Kung
320 University (NCKU).

321

322 **Additional information**

323 Supplementary information is available in the online version of the paper.

324 Correspondence and requests for materials should be addressed to P. G.

325

326 **Competing financial interests**

327 The authors declare no competing financial interests.

328 **List of Captions**

329

330 **Figure 1 | Design principle of vectorial Fourier metasurface for arbitrary far-field**

331 **light distribution of intensity and polarization. (a)** Top view of one pixel of the

332 metasurface. Arbitrary polarization requires superposition of two orthogonal polarizations

333 (chosen here as RCP and LCP) with controllable relative amplitudes and phases. To do so

334 each CP state is produced by two lines of the same handedness with different SOA of $\Delta\delta_{\pm}$

335 to control the relative amplitude and δ_{\pm} to control the relative phase. **(b)** Perspective view

336 of the metasurface and far-field light distribution. The LP input light can be decomposed

337 into two CP beams which are deflected to the same angle of θ_t . The holographic phase

338 information is encoded in the LCP and RCP independently, so that arbitrary polarization

339 is realized by the superposition of the two CP beams. **(c)** Schematic of the intensity and

340 polarization decoupling using vectorial Fourier metasurface. The orientation angle and

341 ellipticity of the polarization exhibiting a “Blade” and a “Rocket” images are encoded in a

342 uniformly distributed intensity profile.

343

344 **Figure 2 | Modified iterative Fourier transform algorithm.** With respect to intensity-

345 only iterative Fourier transform algorithm, the current version considers several input

346 information to realize diffraction patterns with arbitrary intensity, azimuth and ellipticity

347 angles of the polarization. The algorithm converges to a vectorial profile optimizing the

348 amplitude of both LCP (a_{+}^f) and RCP (a_{-}^f), and the phase difference between the two CP

349 beams (α^f). The notation σ represents the handedness of the CP beam, where + or +1

350 represents LCP and – or –1 represents RCP. A random phase of φ_{rd} is used for the

351 starting phase. The number of iterations is $N = 100$. The final holographic phase of the
352 metasurface is φ_{σ}^m . The superscript m indicates the metasurface plane, f is the image plane
353 in the far field. (See more details in Supplementary Note 1)

354

355 **Figure 3 | Simulated results of metasurface with birefringent GaN nanopillars on**
356 **sapphire substrate with dimension of $P = 300$ nm and $h = 1$ μ m. (a) Top view and (b)**
357 **perspective view of one meta-structure. The numerical calculation is performed on unit cell**
358 **of GaN nanopillar on sapphire substrate considering periodic boundary conditions on x and**
359 **y . The width of the GaN nanopillar is fixed as $L_v = 120$ nm. (c) The simulated CP**
360 **conversion by sweeping the length of the GaN nanopillar L_u from 150 nm to 260 nm in the**
361 **wavelength range from 450 nm to 700 nm with zero rotation angle. The dash line represents**
362 **the length of $L_u = 210$ nm. The purple star represents the wavelength at $\lambda = 575$ nm, which**
363 **is the chosen point in **d-f**. (d) The simulated electric field distribution E_x at the plane of x**
364 **$= 0$ and (e) E_y at the plane of $y = 0$. (f) By rotating the GaN nanopillars with an angle of δ**
365 **from 0 to 180°, a near unity CP conversion is shown in the black curve and a geometric**
366 **phase from 0 to 360° is obtained. The simulated results are represented by the blue star, in**
367 **very good agreement with the expected PB phase calculation (red curve).**

368

369 **Figure 4 | Fabricated results and optical measurement of the Stokes Polarization**
370 **parameters of the donut polarization distributed field profile. Field distribution with**
371 **(a) $l = 1, m = 0$, (b) $l = 1, m = 1$, (c) $l = -2, m = 0$, (d) $l = -4, m = 0$. Top row: fabricated**
372 **results with the top view (top panels) and tilt view (bottom panels). The red scale bar**
373 **represents 1 μ m. Second row: Intensity profiles of the designed vectorial fields. The black**

374 arrow represents the local polarization. Third row: measured intensity profiles of the field
375 distributions without linear polarizer. Fourth to seventh rows: measured intensity profiles
376 of the field distributions with a linear polarizer. The white arrow represents the
377 transmission axis of the linear polarizer.

378

379 **Figure 5 | Complex amplitude and polarization information of far field as retrieved**
380 **by the ptychographic measurement.** Measured complex amplitude of (a) x-pol., (b) y-
381 pol., (c) LCP and (d) RCP components. The phase profiles for the four polarization
382 components show typical speckle phase distributions. The inset figure in (d) is the color
383 bar with phase encoded as hue and amplitude as brightness. Measured (e) azimuth angle
384 and (f) ellipticity angle of polarization information.

385

386 **Figure 6 | Broadband characterization of the vectorial metasurfaces designed for a**
387 **field profiles with $l = -2$, $m = 0$.** The measured intensity profiles at different wavelengths
388 of (a) $\lambda = 475$ nm, (b) $\lambda = 525$ nm, (c) $\lambda = 575$ nm, (d) $\lambda = 625$ nm, (e) $\lambda = 675$ nm. Top
389 row: measured intensity profiles without linear polarizer. Second to fifth rows: measured
390 intensity profiles with a linear polarizer. The white arrow represents the transmission axis
391 of the linear polarizer.

392

393 **Figure 7 | Measurement results of vectorial encoded images.** (a)-(c) show the data
394 obtained for the first metasurface design. (d)-(f) correspond to the data for the second
395 metasurface design. (a)-(f) Measurement results using conventional optical setup to image
396 the Stokes parameters. (a) and (d) Measured intensity, (b) and (e) azimuth angle, (c) and

397 (f) ellipticity angle of the polarization. Both interfaces encode a similar uniformly
398 distributed intensity profile as shown in (a) and (d). Color coded images displaying the
399 ellipticity and the orientation, images reveal a “Blade”, a “Rocket”, a “Tree” and a
400 “Squirrel” encoded polarization images as shown in (b), (c), (e) and (f).

401

402 References

403

- 404 (1) Yu, N.; Genevet, P.; Kats, M. A.; Aieta, F.; Tetienne, J.-P.; Capasso, F.; Gaburro,
405 Z. Light Propagation with Phase Discontinuities: Generalized Laws of Reflection
406 and Refraction. *Science* **2011**, *334*, 333–337.
- 407 (2) Lalanne, P.; Astilean, S.; Chavel, P.; Cambril, E.; Launois, H. Blazed Binary
408 Subwavelength Gratings with Efficiencies Larger than Those of Conventional
409 Échelette Gratings. *Opt. Lett.* **1998**, *23*, 1081.
- 410 (3) Genevet, P.; Capasso, F.; Aieta, F.; Khorasaninejad, M.; Devlin, R. Recent
411 Advances in Planar Optics: From Plasmonic to Dielectric Metasurfaces. *Optica*
412 **2017**, *4*, 139.
- 413 (4) Lalanne, P.; Chavel, P. Metalenses at Visible Wavelengths: Past, Present,
414 Perspectives: Metalenses at Visible Wavelengths: Past, Present, Perspectives.
415 *Laser & Photonics Reviews* **2017**, *11* (3), 1600295.
- 416 (5) Chen, H.-T.; Taylor, A. J.; Yu, N. A Review of Metasurfaces: Physics and
417 Applications. *Reports on Progress in Physics* **2016**, *79* (7), 076401.
418 <https://doi.org/10.1088/0034-4885/79/7/076401>.
- 419 (6) Zheng, G.; Mühlenbernd, H.; Kenney, M.; Li, G.; Zentgraf, T.; Zhang, S.
420 Metasurface Holograms Reaching 80% Efficiency. *Nature Nanotechnology* **2015**,
421 *10* (4), 308–312. <https://doi.org/10.1038/nnano.2015.2>.
- 422 (7) Wang, S.; Wu, P. C.; Su, V.-C.; Lai, Y.-C.; Chen, M.-K.; Kuo, H. Y.; Chen, B. H.;
423 Chen, Y. H.; Huang, T.-T.; Wang, J.-H.; Lin, R.-M.; Kuan, C.-H.; Li, T.; Wang,
424 Z.; Zhu, S.; Tsai, D. P. A Broadband Achromatic Metalens in the Visible. *Nature*
425 *Nanotechnology* **2018**, *13* (3), 227–232. [https://doi.org/10.1038/s41565-017-0052-](https://doi.org/10.1038/s41565-017-0052-4)
426 [4](https://doi.org/10.1038/s41565-017-0052-4).
- 427 (8) Huang, L.; Chen, X.; Mühlenbernd, H.; Zhang, H.; Chen, S.; Bai, B.; Tan, Q.; Jin,
428 G.; Cheah, K.-W.; Qiu, C.-W.; Li, J.; Zentgraf, T.; Zhang, S. Three-Dimensional
429 Optical Holography Using a Plasmonic Metasurface. *Nature Communications*
430 **2013**, *4* (1). <https://doi.org/10.1038/ncomms3808>.
- 431 (9) Bomzon, Z.; Biener, G.; Kleiner, V.; Hasman, E. Space-Variant Pancharatnam–
432 Berry Phase Optical Elements with Computer-Generated Subwavelength Gratings.
433 *Opt. Lett.* **2002**, *27* (13), 1141. <https://doi.org/10.1364/OL.27.001141>.
- 434 (10) Yan, L.; Zhu, W.; Karim, M. F.; Cai, H.; Gu, A. Y.; Shen, Z.; Chong, P. H. J.;
435 Kwong, D.-L.; Qiu, C.-W.; Liu, A. Q. $0.2 \lambda_0$ Thick Adaptive Retroreflector Made
436 of Spin-Locked Metasurface. *Advanced Materials* **2018**, *30* (39), 1802721.
437 <https://doi.org/10.1002/adma.201802721>.
- 438 (11) Song, Q. H.; Wu, P. C.; Zhu, W. M.; Zhang, W.; Shen, Z. X.; Chong, P. H. J.;
439 Liang, Q. X.; Tsai, D. P.; Bourouina, T.; Leprince-Wang, Y.; Liu, A. Q. Split
440 Archimedean Spiral Metasurface for Controllable GHz Asymmetric Transmission.
441 *Applied Physics Letters* **2019**, *114* (15), 151105.
442 <https://doi.org/10.1063/1.5084329>.
- 443 (12) Lassaline, N.; Brechbühler, R.; Vonk, S. J. W.; Ridderbeek, K.; Spieser, M.; Bisig,
444 S.; le Feber, B.; Rabouw, F. T.; Norris, D. J. Optical Fourier Surfaces. *Nature*
445 **2020**, *582* (7813), 506–510. <https://doi.org/10.1038/s41586-020-2390-x>.
- 446 (13) Deng, Z.-L.; Deng, J.; Zhuang, X.; Wang, S.; Li, K.; Wang, Y.; Chi, Y.; Ye, X.;
447 Xu, J.; Wang, G. P.; Zhao, R.; Wang, X.; Cao, Y.; Cheng, X.; Li, G.; Li, X.

- 448 Diatomic Metasurface for Vectorial Holography. *Nano Letters* **2018**, *18* (5), 2885–
449 2892. <https://doi.org/10.1021/acs.nanolett.8b00047>.
- 450 (14) Deng, Z.-L.; Deng, J.; Zhuang, X.; Wang, S.; Shi, T.; Wang, G. P.; Wang, Y.; Xu,
451 J.; Cao, Y.; Wang, X.; Cheng, X.; Li, G.; Li, X. Facile Metagrating Holograms
452 with Broadband and Extreme Angle Tolerance. *Light: Science & Applications*
453 **2018**, *7* (1). <https://doi.org/10.1038/s41377-018-0075-0>.
- 454 (15) Song, Q.; Baroni, A.; Sawant, R.; Ni, P.; Brandli, V.; Chenot, S.; Vézian, S.;
455 Damilano, B.; de Mierry, P.; Khadir, S.; Ferrand, P.; Genevet, P. Ptychography
456 Retrieval of Fully Polarized Holograms from Geometric-Phase Metasurfaces.
457 *Nature Communications* **2020**, *11* (1). <https://doi.org/10.1038/s41467-020-16437-9>.
458
- 459 (16) Arbabi, A.; Horie, Y.; Bagheri, M.; Faraon, A. Dielectric Metasurfaces for
460 Complete Control of Phase and Polarization with Subwavelength Spatial
461 Resolution and High Transmission. *Nature Nanotechnology* **2015**, *10* (11), 937–
462 943. <https://doi.org/10.1038/nnano.2015.186>.
- 463 (17) Arbabi, E.; Kamali, S. M.; Arbabi, A.; Faraon, A. Vectorial Holograms with a
464 Dielectric Metasurface: Ultimate Polarization Pattern Generation. *ACS Photonics*
465 **2019**, *6* (11), 2712–2718. <https://doi.org/10.1021/acsp Photonics.9b00678>.
- 466 (18) Li, Y.; Kreske, K.; Rosen, J. Security and Encryption Optical Systems Based on a
467 Correlator with Significant Output Images. *Appl. Opt., AO* **2000**, *39* (29), 5295–
468 5301. <https://doi.org/10.1364/AO.39.005295>.
- 469 (19) Han, J.; Park, C.-S.; Ryu, D.-H.; Kim, E.-S. Optical Image Encryption Based on
470 XOR Operations. *OE* **1999**, *38* (1), 47–54. <https://doi.org/10.1117/1.602060>.
- 471 (20) Tajahuerce, E.; Matoba, O.; Verrall, S. C.; Javidi, B. Optoelectronic Information
472 Encryption with Phase-Shifting Interferometry. *Appl. Opt., AO* **2000**, *39* (14),
473 2313–2320. <https://doi.org/10.1364/AO.39.002313>.
- 474 (21) Javidi, B.; Nomura, T. Polarization Encoding for Optical Security Systems; Javidi,
475 B., Psaltis, D., Eds.; Denver, CO, 1999; pp 196–203.
476 <https://doi.org/10.1117/12.363965>.
- 477 (22) Unnikrishnan, G.; Pohit, M.; Singh, K. A Polarization Encoded Optical Encryption
478 System Using Ferroelectric Spatial Light Modulator. *Optics Communications*
479 **2000**, *185* (1–3), 25–31. [https://doi.org/10.1016/S0030-4018\(00\)00977-9](https://doi.org/10.1016/S0030-4018(00)00977-9).
- 480 (23) Lippmann, G. Sur la théorie de la photographie des couleurs simples et composées
481 par la méthode interférentielle. *J. Phys. Theor. Appl.* **1894**, *3* (1), 97–107.
482 <https://doi.org/10.1051/jphystap:01894003009700>.
- 483 (24) Bryngdahl, O.; Wyrowski, F. I Digital Holography – Computer-Generated
484 Holograms. In *Progress in Optics*; Wolf, E., Ed.; Elsevier, 1990; Vol. 28, pp 1–86.
485 [https://doi.org/10.1016/S0079-6638\(08\)70288-9](https://doi.org/10.1016/S0079-6638(08)70288-9).
- 486 (25) Javidi, B.; Nomura, T. Securing Information by Use of Digital Holography. *Opt.*
487 *Let., OL* **2000**, *25* (1), 28–30. <https://doi.org/10.1364/OL.25.000028>.
- 488 (26) Huang, L.; Zhang, S.; Zentgraf, T. Metasurface Holography: From Fundamentals
489 to Applications. *Nanophotonics* **2018**, *7* (6), 1169–1190.
490 <https://doi.org/10.1515/nanoph-2017-0118>.
- 491 (27) Genevet, P.; Capasso, F. Holographic Optical Metasurfaces: A Review of Current
492 Progress. *Reports on Progress in Physics* **2015**, *78* (2), 024401.
493 <https://doi.org/10.1088/0034-4885/78/2/024401>.

- 494 (28) Deng, Z.-L.; Li, G. Metasurface Optical Holography. *Materials Today Physics*
495 **2017**, *3*, 16–32. <https://doi.org/10.1016/j.mtphys.2017.11.001>.
- 496 (29) Wan, W.; Gao, J.; Yang, X. Metasurface Holograms for Holographic Imaging.
497 *Advanced Optical Materials* **2017**, *5* (21), 1700541.
498 <https://doi.org/10.1002/adom.201700541>.
- 499 (30) Huang, L.; Chen, X.; Mühlenbernd, H.; Zhang, H.; Chen, S.; Bai, B.; Tan, Q.; Jin,
500 G.; Cheah, K.-W.; Qiu, C.-W.; Li, J.; Zentgraf, T.; Zhang, S. Three-Dimensional
501 Optical Holography Using a Plasmonic Metasurface. *Nature Communications*
502 **2013**, *4* (1). <https://doi.org/10.1038/ncomms3808>.
- 503 (31) Deng, Z.-L.; Zhang, S.; Wang, G. P. A Facile Grating Approach towards
504 Broadband, Wide-Angle and High-Efficiency Holographic Metasurfaces.
505 *Nanoscale* **2016**, *8* (3), 1588–1594. <https://doi.org/10.1039/C5NR07181J>.
- 506 (32) Song, Q.; Khadir, S.; Vézian, S.; Damilano, B.; de Mierry, P.; Chenot, S.; Brandli,
507 V.; Laberdesque, R.; Wattellier, B.; Genevet, P. Printing Polarization and Phase at
508 the Optical Diffraction Limit: Near- and Far-Field Optical Encryption. 8.
- 509 (33) Luo, X.; Hu, Y.; Li, X.; Jiang, Y.; Wang, Y.; Dai, P.; Liu, Q.; Shu, Z.; Duan, H.
510 Integrated Metasurfaces with Microprints and Helicity-Multiplexed Holograms for
511 Real-Time Optical Encryption. *Advanced Optical Materials* **2020**, *8* (8), 1902020.
512 <https://doi.org/10.1002/adom.201902020>.
- 513 (34) Zhao, R.; Huang, L.; Tang, C.; Li, J.; Li, X.; Wang, Y.; Zentgraf, T. Nanoscale
514 Polarization Manipulation and Encryption Based on Dielectric Metasurfaces.
515 *Advanced Optical Materials* **2018**, *6* (19), 1800490.
516 <https://doi.org/10.1002/adom.201800490>.
- 517 (35) Zhao, R.; Sain, B.; Wei, Q.; Tang, C.; Li, X.; Weiss, T.; Huang, L.; Wang, Y.;
518 Zentgraf, T. Multichannel Vectorial Holographic Display and Encryption. *Light:*
519 *Science & Applications* **2018**, *7* (1). <https://doi.org/10.1038/s41377-018-0091-0>.
- 520 (36) Deng, J.; Deng, L.; Guan, Z.; Tao, J.; Li, G.; Li, Z.; Li, Z.; Yu, S.; Zheng, G.
521 Multiplexed Anticounterfeiting Meta-Image Displays with Single-Sized
522 Nanostructures. *Nano Letters* **2020**, *20* (3), 1830–1838.
523 <https://doi.org/10.1021/acs.nanolett.9b05053>.
- 524 (37) Khorasaninejad, M.; Ambrosio, A.; Kanhaiya, P.; Capasso, F. Broadband and
525 Chiral Binary Dielectric Meta-Holograms. *Science Advances* **2016**, *2* (5),
526 e1501258. <https://doi.org/10.1126/sciadv.1501258>.
- 527 (38) Chen, K.; Ding, G.; Hu, G.; Jin, Z.; Zhao, J.; Feng, Y.; Jiang, T.; Alù, A.; Qiu, C.
528 Directional Janus Metasurface. *Advanced Materials* **2020**, *32* (2), 1906352.
529 <https://doi.org/10.1002/adma.201906352>.
- 530 (39) Chen, Y.; Yang, X.; Gao, J. 3D Janus Plasmonic Helical Nanoapertures for
531 Polarization-Encrypted Data Storage. *Light: Science & Applications* **2019**, *8* (1).
532 <https://doi.org/10.1038/s41377-019-0156-8>.
- 533 (40) Frese, D.; Wei, Q.; Wang, Y.; Huang, L.; Zentgraf, T. Nonreciprocal Asymmetric
534 Polarization Encryption by Layered Plasmonic Metasurfaces. *Nano Letters* **2019**,
535 *19* (6), 3976–3980. <https://doi.org/10.1021/acs.nanolett.9b01298>.
- 536 (41) Yoon, G.; Lee, D.; Nam, K. T.; Rho, J. “Crypto-Display” in Dual-Mode
537 Metasurfaces by Simultaneous Control of Phase and Spectral Responses. *ACS*
538 *Nano* **2018**, *12* (7), 6421–6428. <https://doi.org/10.1021/acs.nano.8b01344>.

- 539 (42) Tang, Y.; Intaravanne, Y.; Deng, J.; Li, K. F.; Chen, X.; Li, G. Nonlinear Vectorial
540 Metasurface for Optical Encryption. *Phys. Rev. Applied* **2019**, *12* (2), 024028.
541 <https://doi.org/10.1103/PhysRevApplied.12.024028>.
- 542 (43) Deng, J.; Yang, Y.; Tao, J.; Deng, L.; Liu, D.; Guan, Z.; Li, G.; Li, Z.; Yu, S.;
543 Zheng, G.; Li, Z.; Zhang, S. Spatial Frequency Multiplexed Meta-Holography and
544 Meta-Nanoprinting. *ACS Nano* **2019**. <https://doi.org/10.1021/acsnano.9b03738>.
- 545 (44) Ren, H.; Briere, G.; Fang, X.; Ni, P.; Sawant, R.; Héron, S.; Chenot, S.; Vézian, S.;
546 Damilano, B.; Brändli, V.; Maier, S. A.; Genevet, P. Metasurface Orbital Angular
547 Momentum Holography. *Nature Communications* **2019**, *10* (1).
548 <https://doi.org/10.1038/s41467-019-11030-1>.
- 549 (45) Fang, X.; Ren, H.; Gu, M. Orbital Angular Momentum Holography for High-
550 Security Encryption. *Nature Photonics* **2020**, *14* (2), 102–108.
551 <https://doi.org/10.1038/s41566-019-0560-x>.
- 552 (46) Li, J.; Kamin, S.; Zheng, G.; Neubrech, F.; Zhang, S.; Liu, N. Addressable
553 Metasurfaces for Dynamic Holography and Optical Information Encryption.
554 *Science Advances* **2018**, *4* (6), eaar6768. <https://doi.org/10.1126/sciadv.aar6768>.
- 555 (47) Zhou, H.; Wang, Y.; Li, X.; Wang, Q.; Wei, Q.; Geng, G.; Huang, L. Switchable
556 Active Phase Modulation and Holography Encryption Based on Hybrid
557 Metasurfaces. *Nanophotonics* **2020**, *9* (4), 905–912.
558 <https://doi.org/10.1515/nanoph-2019-0519>.
- 559 (48) Vyas, S.; Kozawa, Y.; Sato, S. Polarization Singularities in Superposition of
560 Vector Beams. *Optics Express* **2013**, *21* (7), 8972.
561 <https://doi.org/10.1364/OE.21.008972>.
- 562 (49) Zhan, Q. Cylindrical Vector Beams: From Mathematical Concepts to Applications.
563 *Advances in Optics and Photonics* **2009**, *1* (1), 1.
564 <https://doi.org/10.1364/AOP.1.000001>.
- 565 (50) Schaefer, B.; Collett, E.; Smyth, R.; Barrett, D.; Fraher, B. Measuring the Stokes
566 Polarization Parameters. *American Journal of Physics* **2007**, *75* (2), 163–168.
567 <https://doi.org/10.1119/1.2386162>.
- 568 (51) Rubin, N. A.; D’Aversa, G.; Chevalier, P.; Shi, Z.; Chen, W. T.; Capasso, F.
569 Matrix Fourier Optics Enables a Compact Full-Stokes Polarization Camera.
570 *Science* **2019**, *365* (6448). <https://doi.org/10.1126/science.aax1839>.
- 571 (52) Baroni, A.; Allain, M.; Li, P.; Chamard, V.; Ferrand, P. Joint Estimation of Object
572 and Probes in Vectorial Ptychography. *Optics Express* **2019**, *27* (6), 8143.
573 <https://doi.org/10.1364/OE.27.008143>.
- 574 (53) Ferrand, P.; Allain, M.; Chamard, V. Ptychography in Anisotropic Media. *Optics*
575 *Letters* **2015**, *40* (22), 5144. <https://doi.org/10.1364/OL.40.005144>.
- 576 (54) Ferrand, P.; Baroni, A.; Allain, M.; Chamard, V. Quantitative Imaging of
577 Anisotropic Material Properties with Vectorial Ptychography. *Optics Letters* **2018**,
578 *43* (4), 763. <https://doi.org/10.1364/OL.43.000763>.

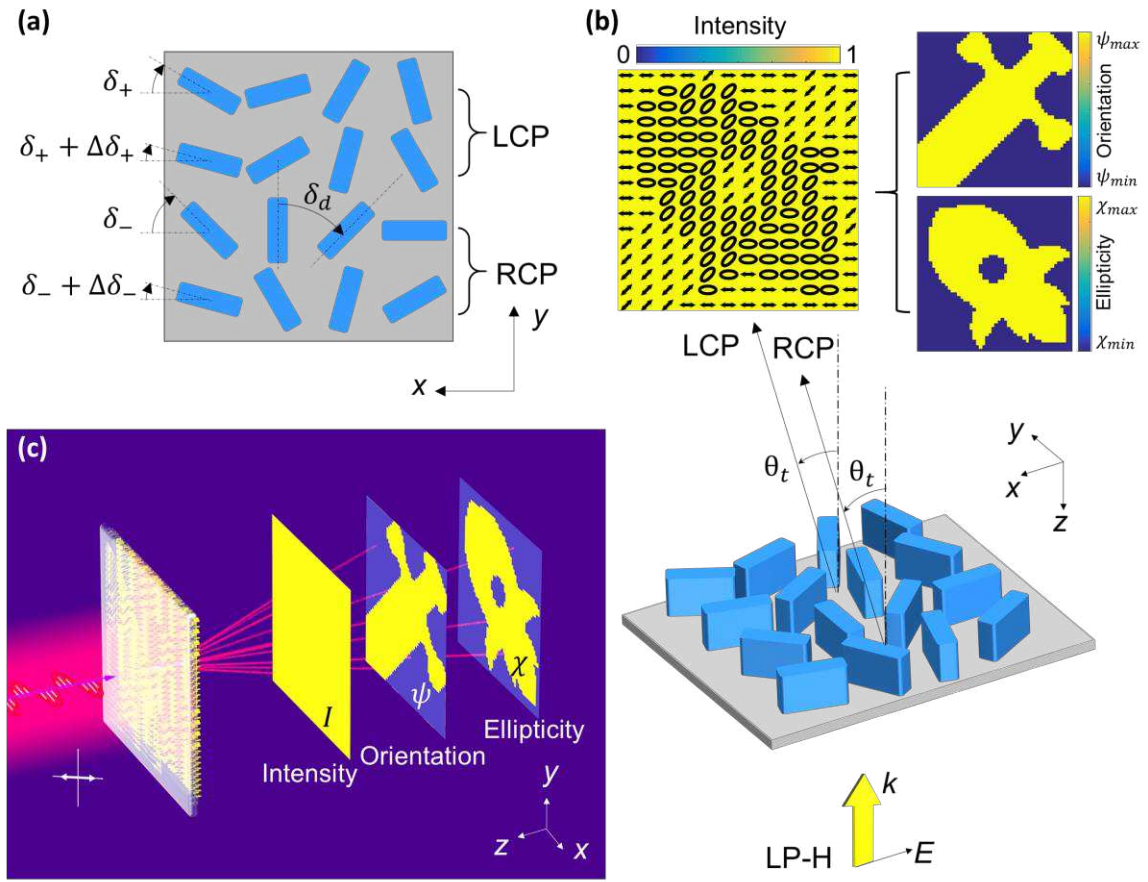


Figure 1

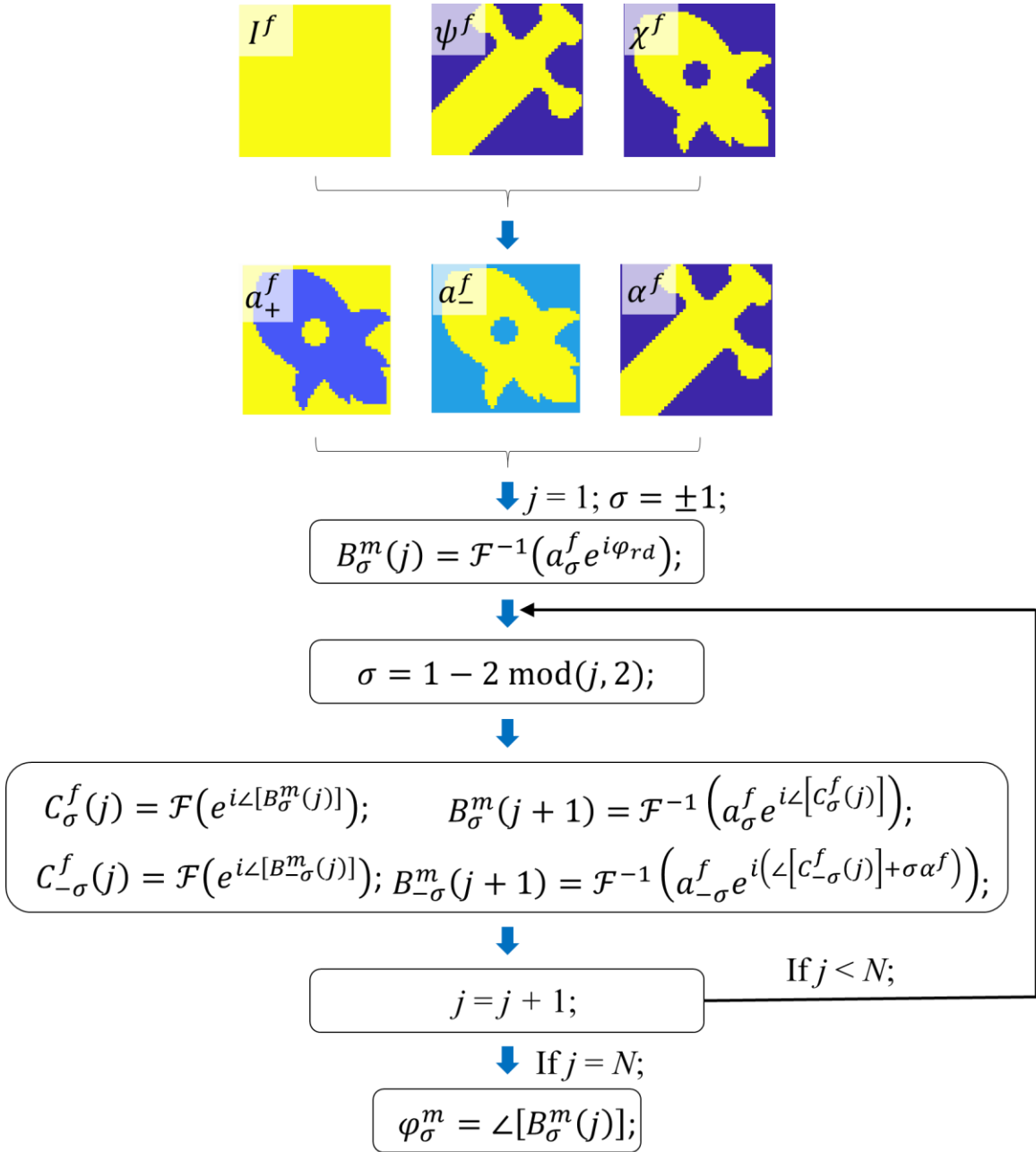


Figure 2

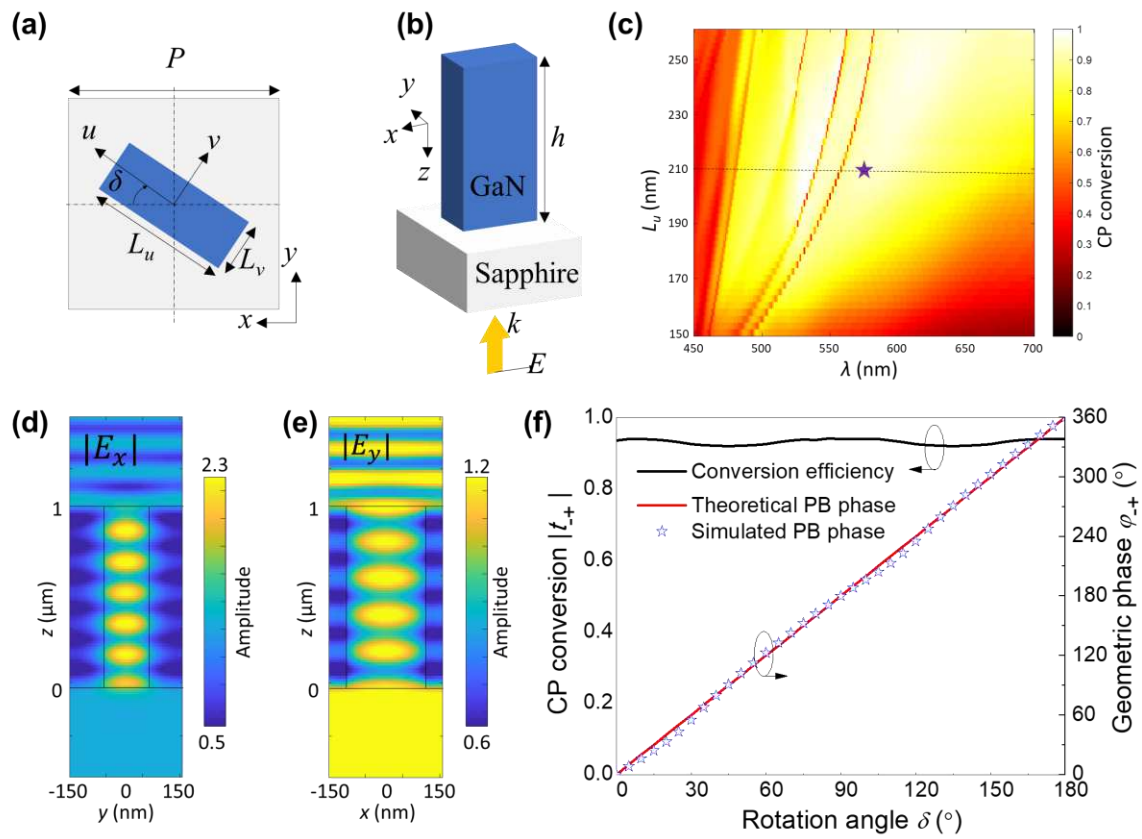


Figure 3

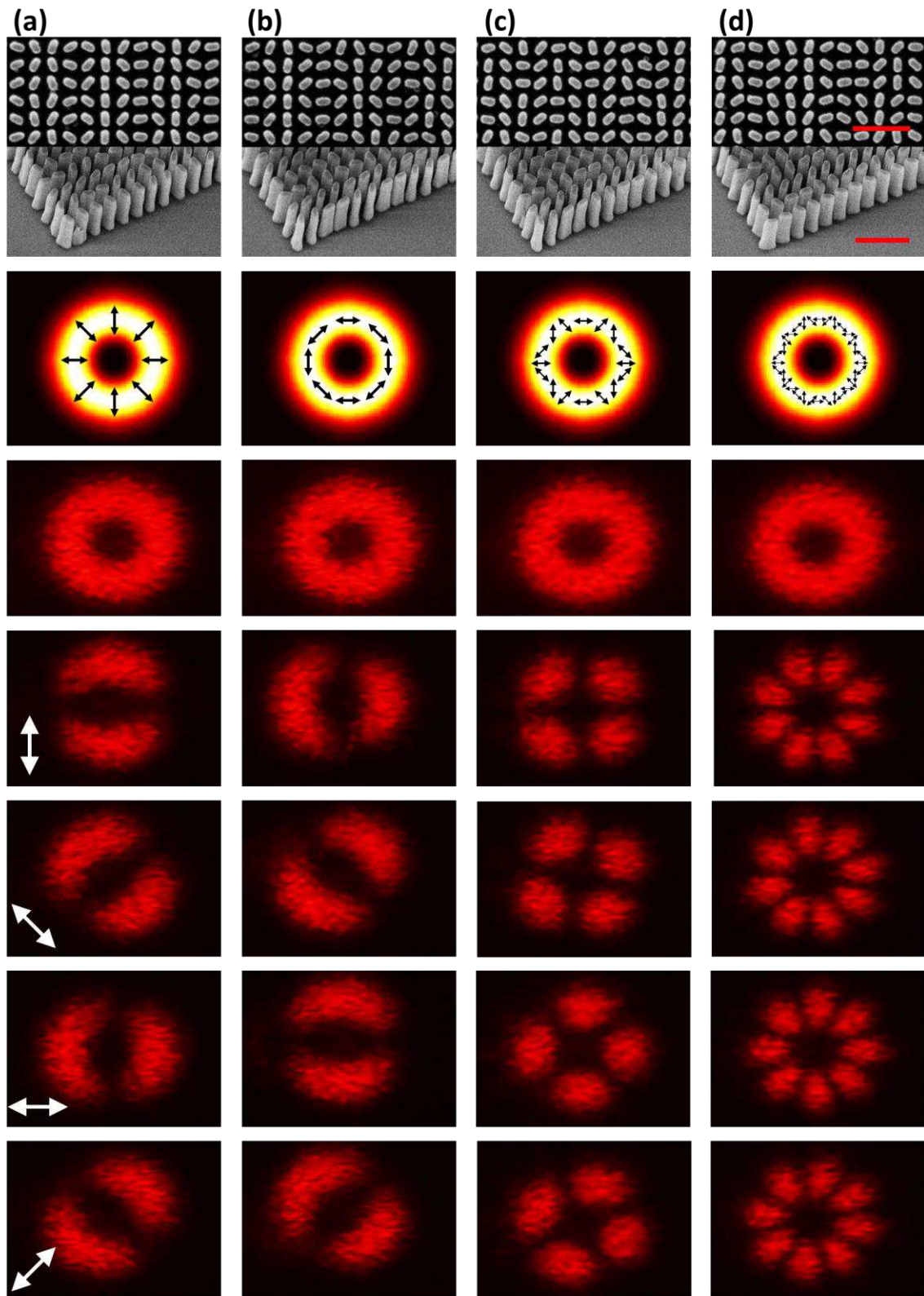


Figure 4

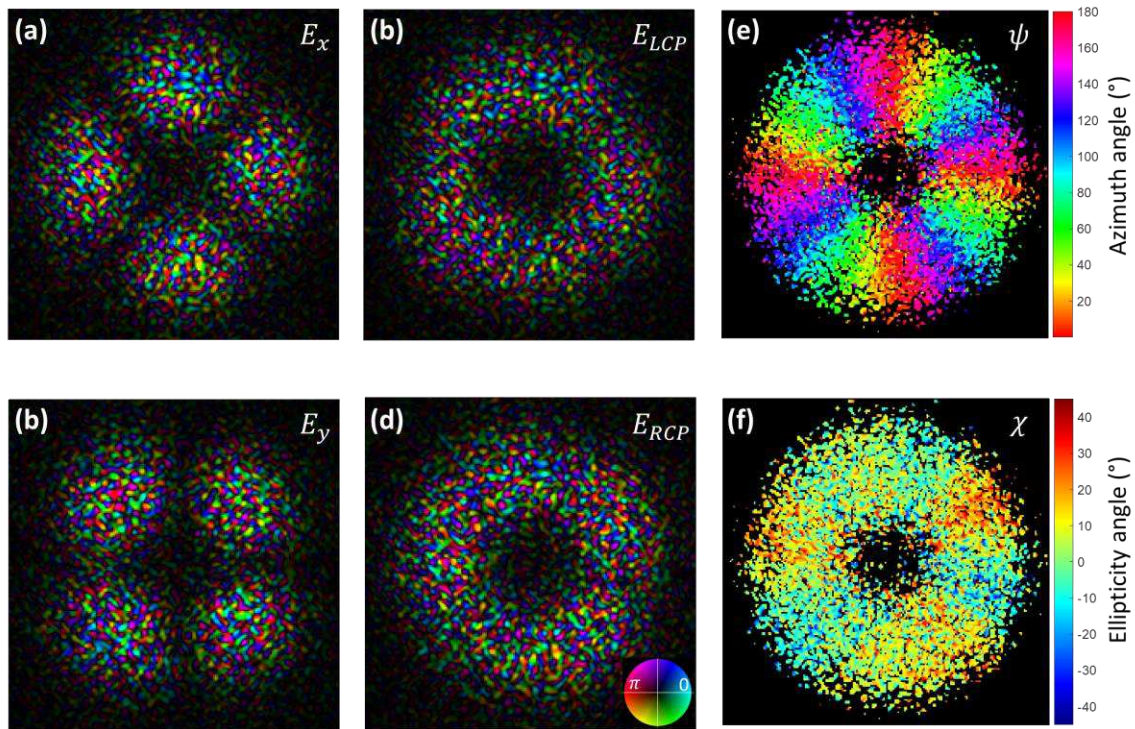


Figure 5

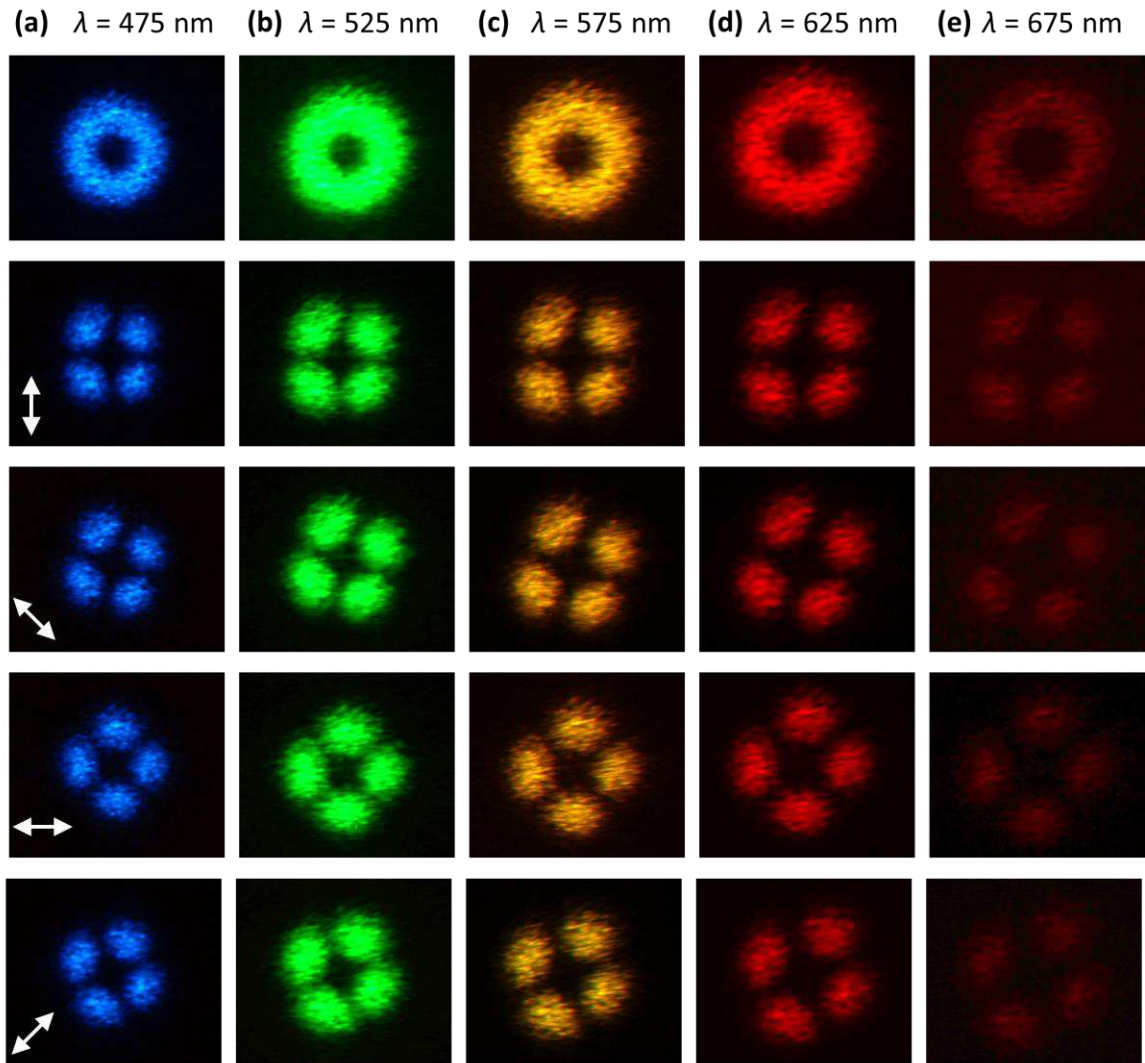


Figure 6

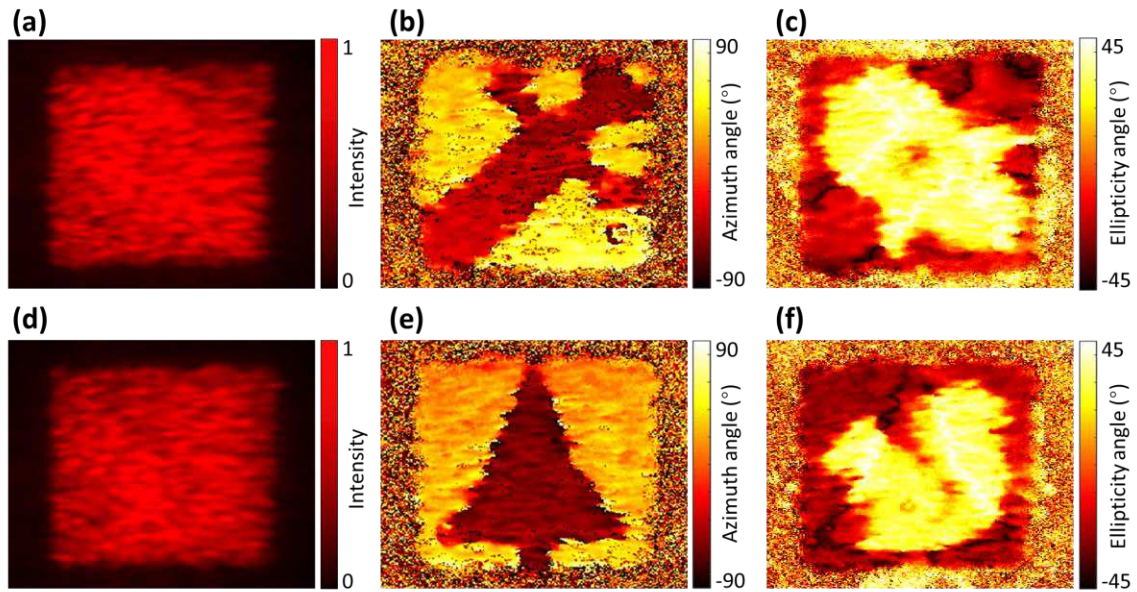


Figure 7

Supplementary Information

581

582

583

Broadband Decoupling of Intensity and Polarization with Vectorial Fourier Metasurfaces

586

587 Qinghua Song¹, Arthur Baroni², Pin Chieh Wu³, Sébastien Chenot¹, Virginie Brandli¹,
588 Stéphane Vézian¹, Benjamin Damilano¹, Philippe de Mierry¹, Samira Khadir¹, Patrick
589 Ferrand² and Patrice Genevet^{1†}

590

591 ¹ *Université Cote d'Azur, CNRS, CRHEA, Rue Bernard Gregory, Sophia Antipolis 06560*
592 *Valbonne, France*

593 ² *Aix Marseille univ, CNRS, Centrale Marseille, Institut Fresnel, 13013 Marseille,*
594 *France*

595 ³ *Department of Photonics, National Cheng Kung University, Tainan 70101, Taiwan*

596

597 [†] *Corresponding Author: Patrice.Genevet@crhea.cnrs.fr*

598 **Supplementary Note 1: Modified iterative Fourier transform algorithm**

599 In order to decouple the amplitude and polarization information, a modified iterative
600 Fourier transform algorithm is used to calculate the holographic phase profile for both LCP
601 and RCP as shown in Figure 2. Assuming an arbitrary far field information with intensity
602 I^f , azimuth angle ψ^f and ellipticity angle χ^f (the superscript f represent the far field image
603 plane, m represent the metasurface plane), it can be converted to the amplitude information
604 for LCP (a_+^f) and RCP (a_-^f), and phase difference between LCP and RCP (α^f) as shown
605 below,

$$606 \quad a_\sigma^f = \sqrt{(I - \sigma I \sin(2\chi))/2} \quad (1)$$

$$607 \quad \alpha^f = 2\psi^f \quad (2)$$

608 where $\sigma = +$ (or $+1$) represents LCP, $\sigma = -$ (or -1) represent RCP. We apply a random
609 phase φ_{rd} into the amplitude information of Eq. S1 to obtain the initial complex amplitude
610 $a_\sigma^f e^{i\varphi_{rd}}$ and perform the inverse Fourier transform to get the initial metasurface
611 information,

$$612 \quad B_\sigma^m(1) = \mathcal{F}^{-1}(a_\sigma^f e^{i\varphi_{rd}}) \quad (3)$$

613 where \mathcal{F} and \mathcal{F}^{-1} are the operators for Fourier transform and inverse Fourier transform,
614 respectively. Considering the amplitude in the metasurface plane for LCP and RCP is
615 constant, an iterative Fourier transform process is used to get the phase information as
616 following. The iteration number j is an integer number starting from 1. If j is an odd number,
617 the algorithm is described as,

$$618 \quad C_-^f(j) = \mathcal{F}(e^{i\angle[B_-^m(j)]}) \quad (4)$$

$$619 \quad B_-^m(j+1) = \mathcal{F}^{-1}(a_-^f e^{i\angle[C_-^f(j)]}) \quad (5)$$

620
$$C_+^f(j) = \mathcal{F}(e^{i\angle[B_+^m(j)]}) \quad (6)$$

621
$$B_+^m(j+1) = \mathcal{F}^{-1}\left(a_-^f e^{i(\angle[C_-^f(j)] - \alpha^f)}\right) \quad (7)$$

622 where $\angle[X]$ represent the phase of complex number X . If j is an even number, the algorithm
 623 becomes,

624
$$C_+^f(j) = \mathcal{F}(e^{i\angle[B_+^m(j)]}) \quad (8)$$

625
$$B_+^m(j+1) = \mathcal{F}^{-1}\left(a_+^f e^{i\angle[C_+^f(j)]}\right) \quad (9)$$

626
$$C_-^f(j) = \mathcal{F}(e^{i\angle[B_-^m(j)]}) \quad (10)$$

627
$$B_-^m(j+1) = \mathcal{F}^{-1}\left(a_+^f e^{i(\angle[C_+^f(j)] + \alpha^f)}\right) \quad (11)$$

628 When the iteration number j reaches a given value N , the iteration process ends. The final
 629 phase information of the metasurface is given as,

630
$$\varphi_\sigma^m = \angle[B_\sigma^m(j)] \quad (12)$$

631 Eq. S4-S12 can be simplified as Figure 2 in the main text.

632 **Supplementary Note 2: Determination of rotation angle of meta-structures**

633 Since the meta-structure with a rotation angle of δ converts the CP light of $|\pm\rangle$ to $|\mp\rangle$ with
 634 geometric phase of $\pm 2\delta$ that is used to encode the holographic phase information, the
 635 rotation angle of the meta-structure is given as,

$$636 \quad \delta_\sigma = -\sigma\varphi_\sigma^m/2 \quad (13)$$

637 Since the intensity of LCP and RCP in the hologram plane are not always equal to each
 638 other, additional freedom should be considered to control the intensity difference between
 639 LCP and RCP. In this paper, we use two lines of LCP and RCP to control the amplitude
 640 according to the interference effect of the two lines. The rotation angles are δ_+ and δ_+ +
 641 $\Delta\delta_+$ for two LCP lines, and δ_- and $\delta_- + \Delta\delta_-$ for two RCP lines as shown in Figure 1A in
 642 the main text. The amplitude of the output LCP and RCP can be given as,

$$643 \quad A_+^m = |e^{-i2\delta_+} + e^{-i2(\delta_+ + \Delta\delta_+)}|/2 = \sqrt{(1 + \cos 2\Delta\delta_+)/2} \quad (14)$$

$$644 \quad A_-^m = |e^{i2\delta_-} + e^{i2(\delta_- + \Delta\delta_-)}|/2 = \sqrt{(1 + \cos 2\Delta\delta_-)/2} \quad (15)$$

645 which can be simplified as Eq. 2 in the main text. The total intensity for LCP and RCP in
 646 the metasurface plane can be described as,

$$647 \quad I_\sigma^m = (A_\sigma^m)^2 \quad (16)$$

$$648 \quad I^m = I_+^m + I_-^m \quad (17)$$

649 Since the intensity of LCP and RCP in the image plane can be calculated from Eq. S1 as,

$$650 \quad I_\sigma^f = \sum_{x,y=1}^{N_x, N_y} \left(a_\sigma^f(x^f, y^f) \right)^2 \quad (18)$$

651 where x^f and y^f represent the coordinate of the pixels in the image plane, N_x and N_y are
 652 the total pixel number in x^f and y^f direction. According to the Eq. S14-S18, and using
 653 the fact that $I_\sigma^m = I_\sigma^f$, we can get the relationship of $\Delta\delta_+$ and $\Delta\delta_-$ as,

654
$$\frac{1+\cos 2\Delta\delta_+}{1+\cos 2\Delta\delta_-} = \frac{\sum_{x,y=1}^{N_x,N_y} (a_+^f(x^f,y^f))^2}{\sum_{x,y=1}^{N_x,N_y} (a_-^f(x^f,y^f))^2} \quad (19)$$

655 There are three possibilities as discussed below:

656 (1) if the intensity $I_+^f = I_-^f$, we choose

657
$$\Delta\delta_+ = \Delta\delta_- = 0 \quad (20)$$

658 (2) if $I_+^f > I_-^f$, we keep $\Delta\delta_+ = 0$ and $\Delta\delta_-$ is calculated from Eq. S19 as,

659
$$\begin{cases} \Delta\delta_+ = 0 \\ \Delta\delta_- = \arccos\left(\frac{2\sum_{x,y=1}^{N_x,N_y} (a_-^f(x^f,y^f))^2}{\sum_{x,y=1}^{N_x,N_y} (a_+^f(x^f,y^f))^2} - 1\right)/2 \end{cases} \quad (21)$$

660 (3) if $I_+^f < I_-^f$, we keep $\Delta\delta_- = 0$ and $\Delta\delta_+$ is calculated from Eq. S19 as,

661
$$\begin{cases} \Delta\delta_+ = \arccos\left(\frac{2\sum_{x,y=1}^{N_x,N_y} (a_+^f(x^f,y^f))^2}{\sum_{x,y=1}^{N_x,N_y} (a_-^f(x^f,y^f))^2} - 1\right)/2 \\ \Delta\delta_- = 0 \end{cases} \quad (22)$$

662 Eq. S20-S22 can be simplified as,

663
$$\begin{cases} \Delta\delta_\sigma = 0, & \text{if } I_\sigma^f \geq I_{-\sigma}^f \\ \Delta\delta_\sigma = \arccos\left(\frac{2\sum_{x,y=1}^{N_x,N_y} (a_\sigma^f(x^f,y^f))^2}{\sum_{x,y=1}^{N_x,N_y} (a_{-\sigma}^f(x^f,y^f))^2} - 1\right)/2, & \text{if } I_\sigma^f < I_{-\sigma}^f \end{cases} \quad (23)$$

664 which is presented in Eq. 4 in the main text.

665 Therefore, the final orientation angle is obtained from Eq. S13 and S23.

666

667 **Supplementary Note 3: Measurement of the polarization parameters**

668 The optical setup of the polarization measurement is shown in Figure S2. A quarter
669 waveplate with its fast axis along the x -axis and a linear polarizer with the transmission
670 axis rotated through an angle of θ with respect to the x -axis is placed before the holographic
671 image. The intensity of the optical beam after the waveplate and linear polarizer is related
672 to the Stokes parameters as [50, 51],

673
$$I(\theta, \phi) = \frac{1}{2}(S_0 + S_1 \cos 2\theta + S_2 \sin 2\theta \cos \phi - S_3 \sin 2\theta \sin \phi) \quad (24)$$

674 where θ is the rotation angle of the linear polarizer and ϕ is the phase of the waveplate.
675 Firstly, we remove the waveplate and measure sequentially the intensity of the output light
676 with the linear polarizer set at $\theta = 0^\circ$, 45° , and 90° , respectively. Then the final (fourth)
677 measurement is carried out with the quarter-waveplate ($\phi = 90^\circ$) together with a linear
678 polarizer set at $\theta = 45^\circ$. From Eq. S24, we can get,

679
$$I(0^\circ, 0^\circ) = \frac{1}{2}(S_0 + S_1) \quad (25)$$

680
$$I(45^\circ, 0^\circ) = \frac{1}{2}(S_0 + S_2) \quad (26)$$

681
$$I(90^\circ, 0^\circ) = \frac{1}{2}(S_0 - S_1) \quad (27)$$

682
$$I(45^\circ, 90^\circ) = \frac{1}{2}(S_0 - S_3) \quad (28)$$

683 Therefore, the Stokes parameter is given by,

684
$$S_0 = I(0^\circ, 0^\circ) + I(90^\circ, 0^\circ) \quad (29)$$

685
$$S_1 = I(0^\circ, 0^\circ) - I(90^\circ, 0^\circ) \quad (30)$$

686
$$S_2 = 2I(45^\circ, 0^\circ) - I(0^\circ, 0^\circ) - I(90^\circ, 0^\circ) \quad (31)$$

687
$$S_3 = I(0^\circ, 0^\circ) + I(90^\circ, 0^\circ) - 2I(45^\circ, 90^\circ) \quad (32)$$

688 The azimuth angle and ellipticity angle can be extracted from the Stokes parameter as,

689
$$\psi = \frac{1}{2} \tan^{-1} \left(\frac{S_2}{S_1} \right) \quad (0 < \psi < \pi) \quad (33)$$

690
$$\chi = \frac{1}{2} \sin^{-1} \left(\frac{S_3}{S_0} \right) \quad \left(-\frac{\pi}{4} < \chi < \frac{\pi}{4} \right) \quad (34)$$

691 Therefore, from Eq. S29-S34, we can calculate azimuth angle and ellipticity angles as,

692
$$\psi = \frac{1}{2} \tan^{-1} \left(\frac{2I(45^\circ, 0^\circ) - I(0^\circ, 0^\circ) - I(90^\circ, 0^\circ)}{I(0^\circ, 0^\circ) - I(90^\circ, 0^\circ)} \right) \quad (0 < \psi < \pi) \quad (35)$$

693
$$\chi = \frac{1}{2} \sin^{-1} \left(\frac{I(0^\circ, 0^\circ) + I(90^\circ, 0^\circ) - 2I(45^\circ, 90^\circ)}{I(0^\circ, 0^\circ) + I(90^\circ, 0^\circ)} \right) \quad \left(-\frac{\pi}{4} < \chi < \frac{\pi}{4} \right) \quad (36)$$

694 which is given in the main text.

695

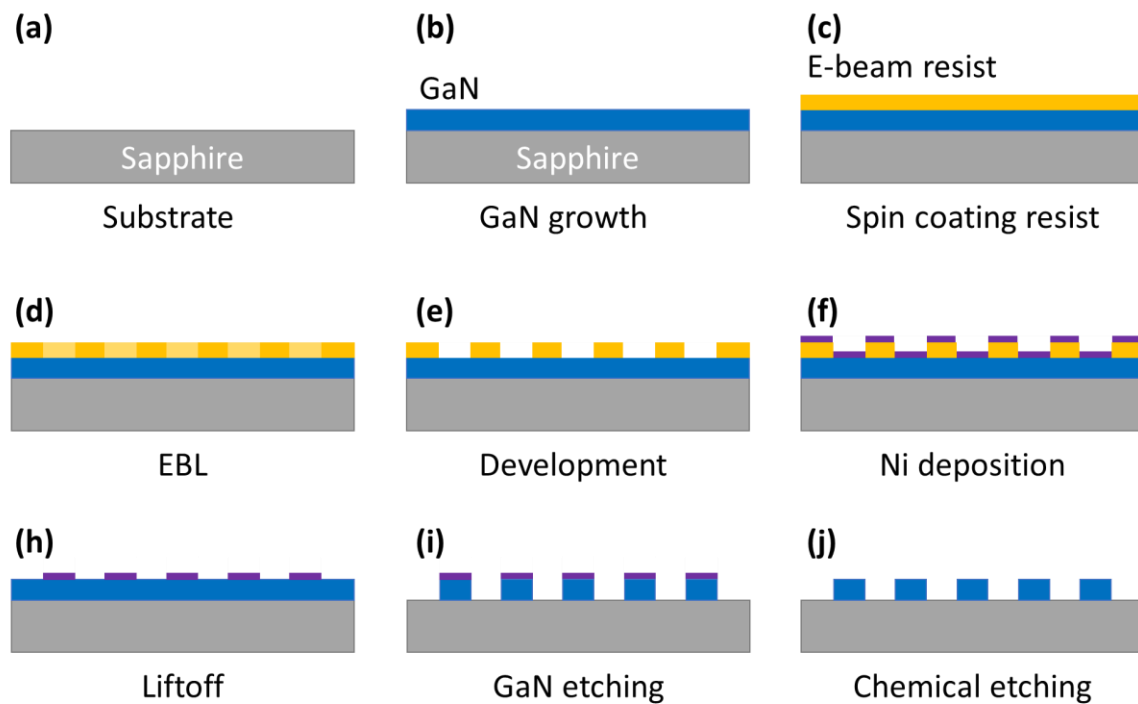


Figure S1. Fabrication processes of metasurface. (A) A double-side polished c-plan sapphire is used as the substrate. (B) GaN thin-film with 1 μm thickness is grown on sapphire substrate. (C) Spin coated with PMMA resist. (D) Exposure using electron beam lithography. (E) Development in 3:1 IPA:MIBK solution. (F) Nickel deposition with 50 nm using E-beam evaporation. (G) Liftoff process in acetone. (H) GaN etching by reactive ion etching. (I) Chemical etching in 1:1 H_2O_2 : H_2SO_4 solution to remove the nickel.

696

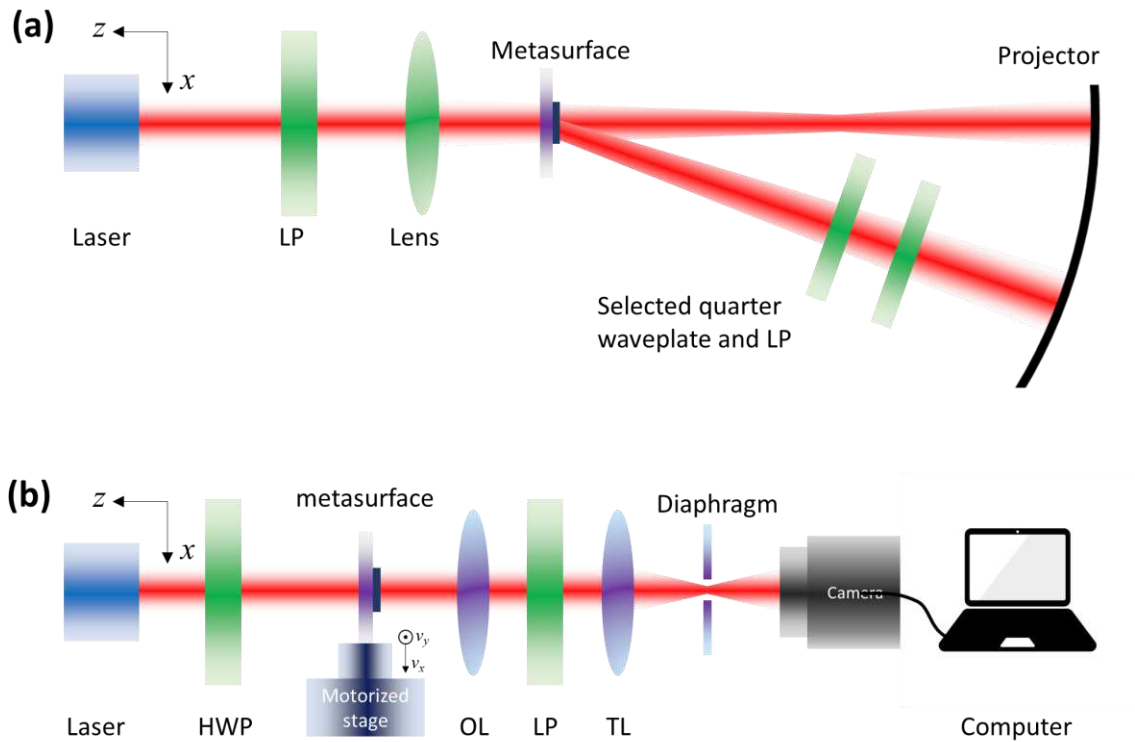


Figure S2. Measurement setup of conventional optical setup and ptychographic optical setup. (a) Schematic of the conventional optical setup. A laser with wavelength of 635 nm is passing through a linear polarizer and lens to weakly focused on the metasurface. A projector with a distance of 10 cm to the metasurface is placed to display the holographic images. Selected quarter waveplate and linear polarizer are placed before the projector to analyze the holographic images and measure the Stokes parameters. (b) Schematic of the ptychographic measurement optical setup. LP: linear polarizer. HWP: half waveplate. OL: objective lens. TL: tube lens.

697

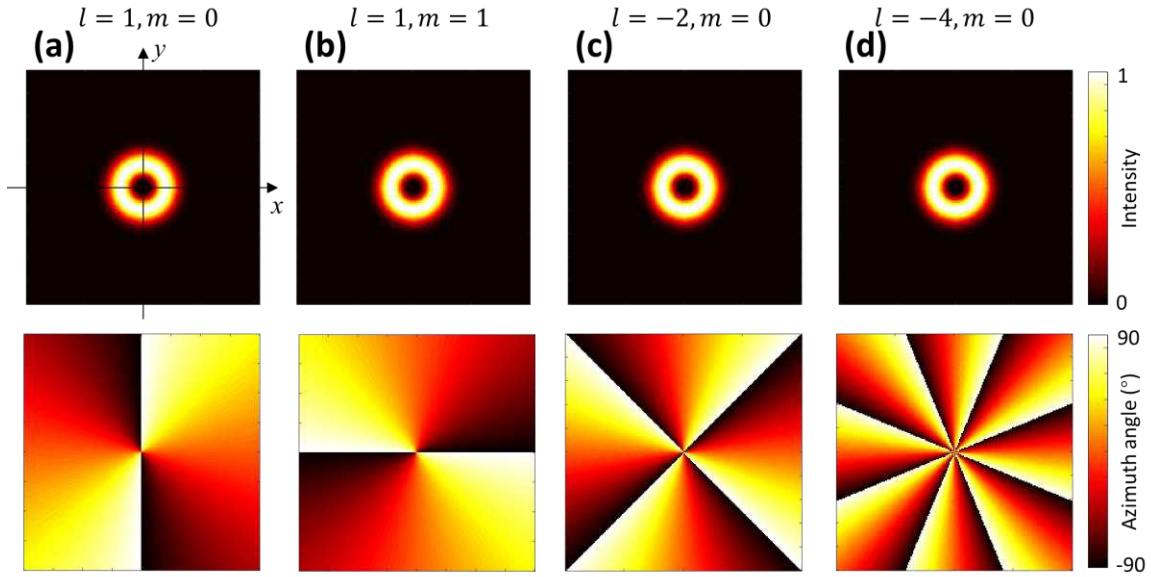


Figure S3. Design of field profile mimicking the cylindrical vector beams. The field profile design with (a) $l = 1, m = 0$, (b) $l = 1, m = 1$, (c) $l = -2, m = 0$, (d) $l = -4, m = 0$. Top row: intensity profile. Bottom row: azimuth angle profile. The ellipticity angle of all of the designs are zero. Note that with respect to CV beams, the far-field phase distribution is not imposed.

698

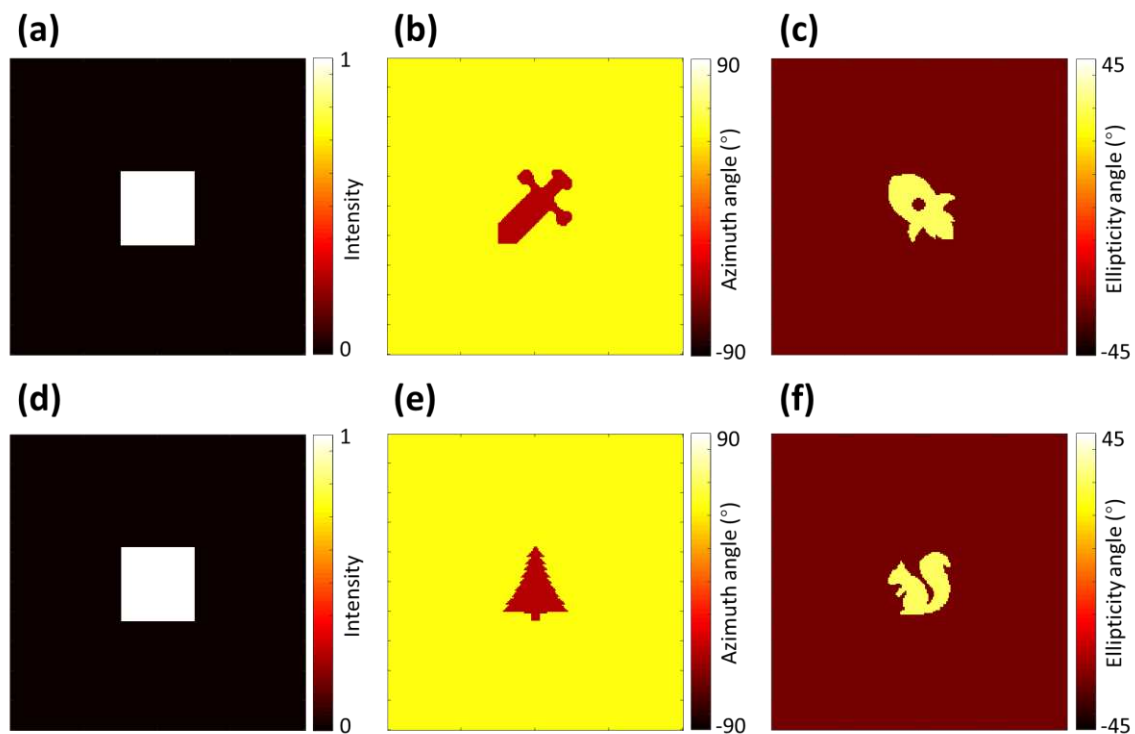


Figure S4. Design of the metasurface for optical encryption. (a) – (c) Metasurface design 1 with uniformly distributed intensity profile in (a), a “Blade” image in (b) and a “Rocket” image in (c). (d) – (f) Metasurface design 2 with uniformly distributed intensity profile in (d), a “Tree” image in (e) and a “Squirrel” image in (f).

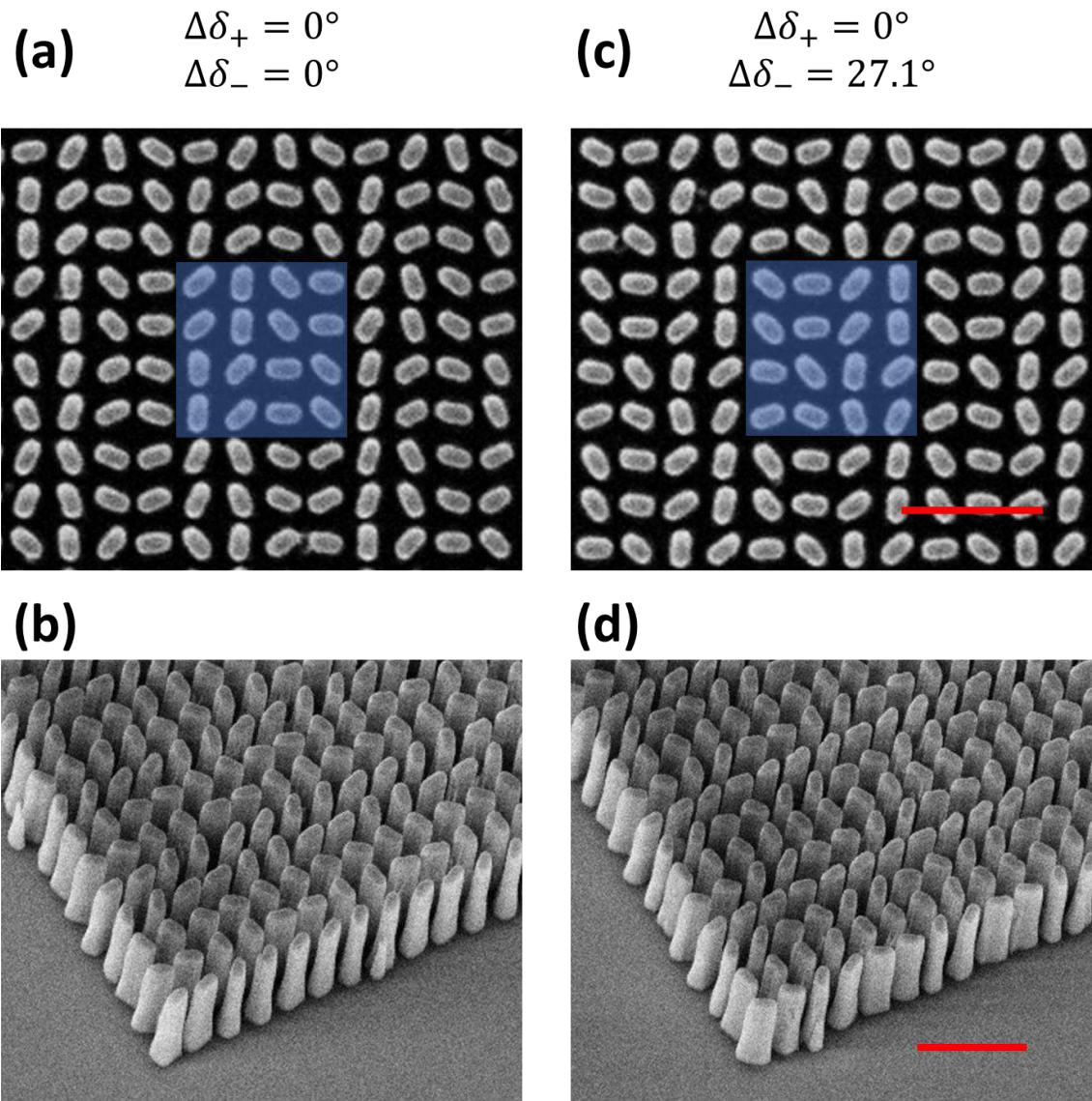


Figure S5. Fabricated results of metasurface design 1 and design 2 for the optical encryption. (a) Top view and (b) tilt view of metasurface design 1 with rotation angle difference of $\Delta\delta_{\pm} = 0^\circ$. (c) Top view and (d) tilt view of metasurface design 2 with rotation angle difference of $\Delta\delta_+ = 0^\circ$ and $\Delta\delta_- = 27.1^\circ$. The red scale bar represents $1\mu\text{m}$.

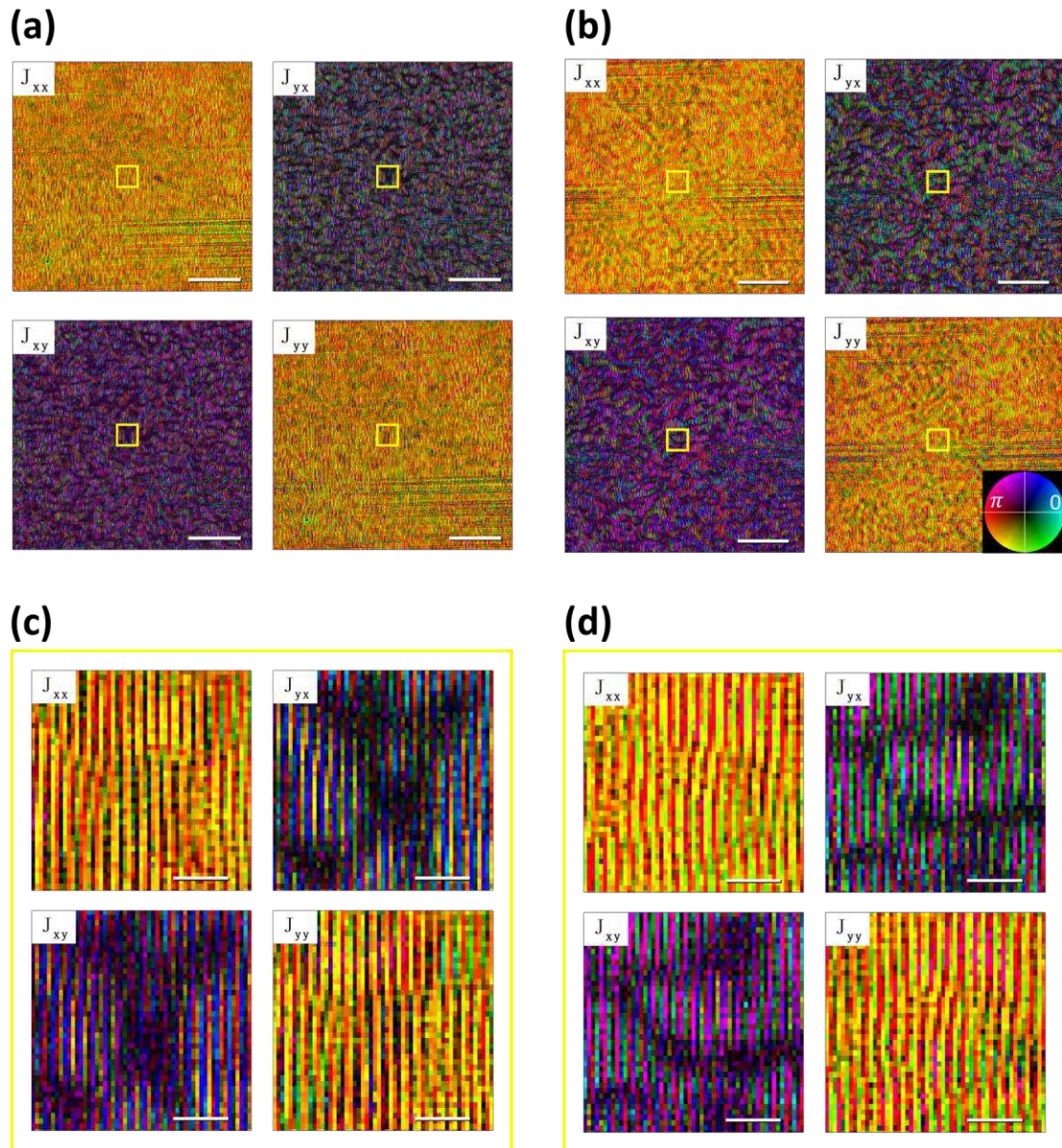


Figure S6. Retrieved Jones matrix through ptychographic measurement. Measured Jones matrix of (a) Metasurface 1 and (b) Metasurface 2. The enlarged images of the central rectangle area are shown in (c) and (d). The inset figure in (b) is the color bar with phase encoded as hue and amplitude as brightness. The scale bar in (a) and (b) is $50 \mu\text{m}$. The scale bar in (a) and (b) is $5 \mu\text{m}$.

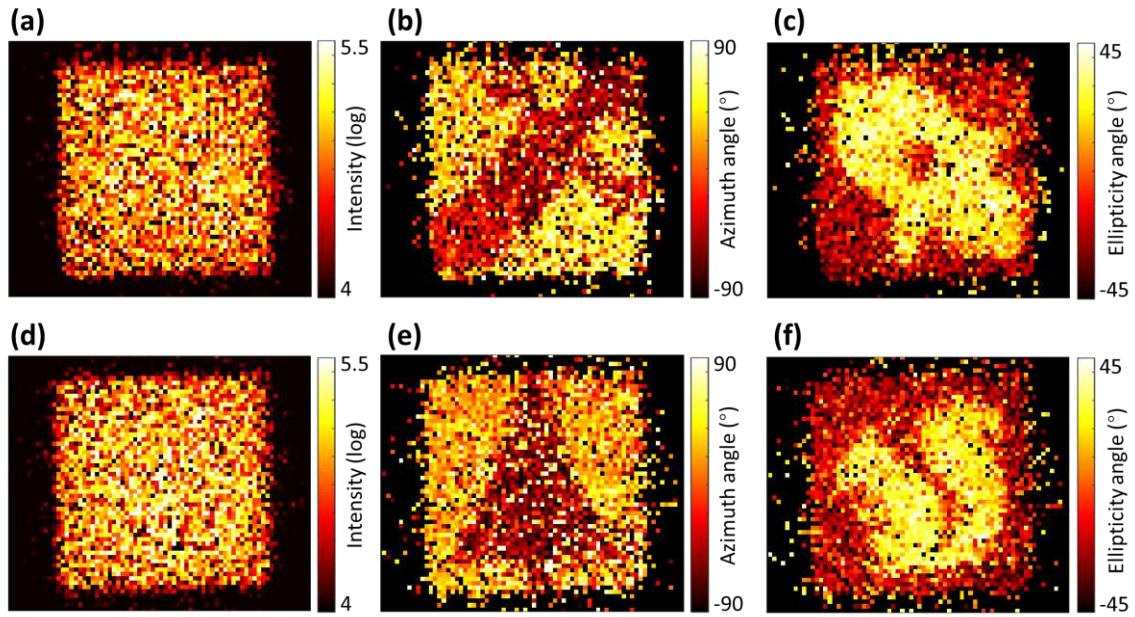


Figure S7. Measurement results of vectorial encoded images using ptychographic measurement. (a) and (d) Retrieved intensity, (b) and (e) azimuth angle, (c) and (f) ellipticity angle of the polarization. A uniformly distributed intensity profile is shown in (a) and (d), a “Blade”, “Rocket”, “Tree” and “Squirrel” images are shown in (b), (c), (e) and (f). The measurement using conventional optical setup and ptychographic setup agree with the design.

Figures

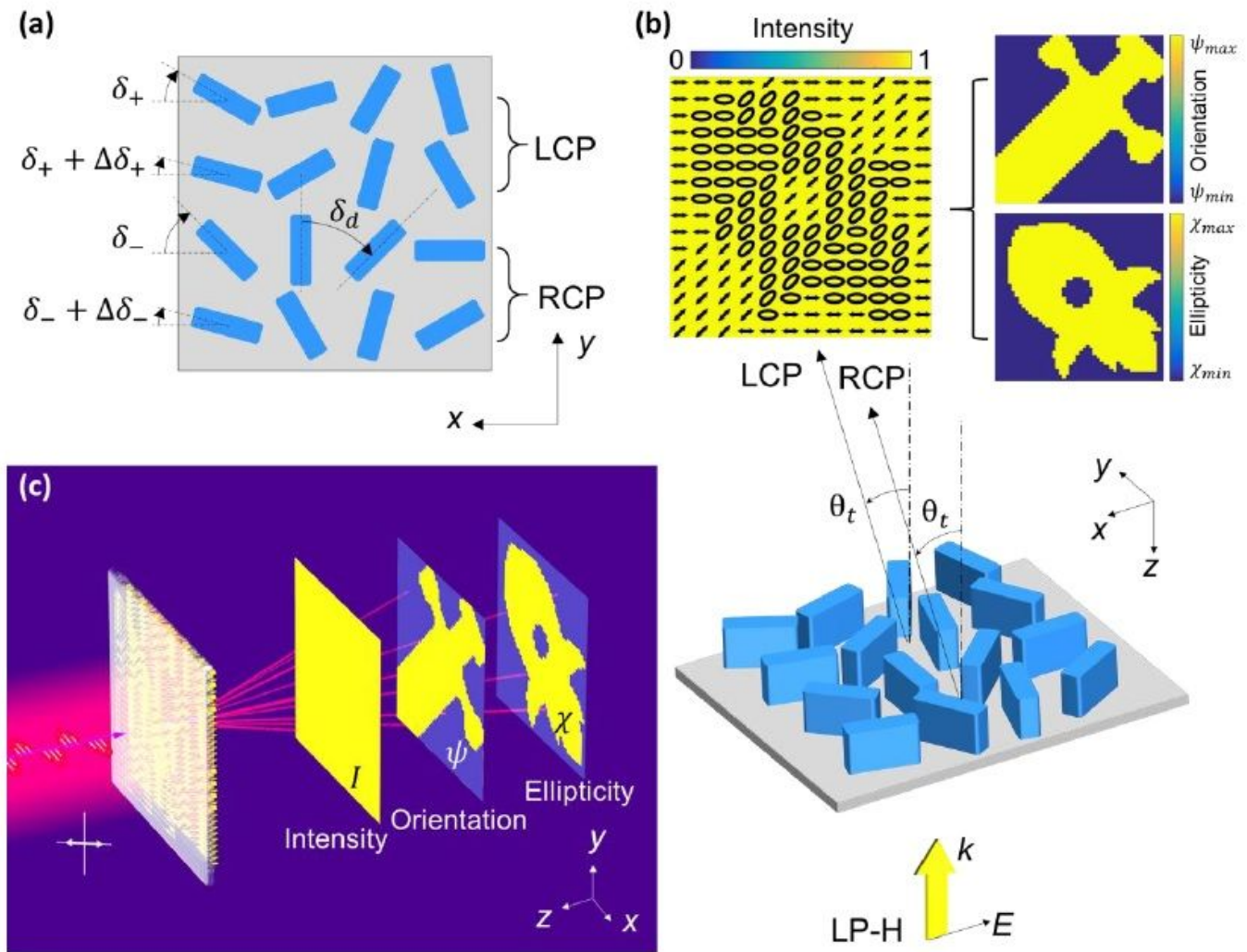


Figure 1

Design principle of vectorial Fourier metasurface for arbitrary far-field light distribution of intensity and polarization. (a) Top view of one pixel of the metasurface. Arbitrary polarization requires superposition of two orthogonal polarizations (chosen here as RCP and LCP) with controllable relative amplitudes and phases. To do so each CP state is produced by two lines of the same handedness with different SOA of $\Delta\delta_{\pm}$ to control the relative amplitude and δ_{\pm} to control the relative phase. (b) Perspective view of the metasurface and far-field light distribution. The LP input light can be decomposed into two CP beams which are deflected to the same angle of θ_t . The holographic phase information is encoded in the LCP and RCP independently, so that arbitrary polarization is realized by the superposition of the two CP beams. (c) Schematic of the intensity and polarization decoupling using vectorial Fourier metasurface. The orientation angle and ellipticity of the polarization exhibiting a “Blade” and a “Rocket” images are encoded in a uniformly distributed intensity profile.

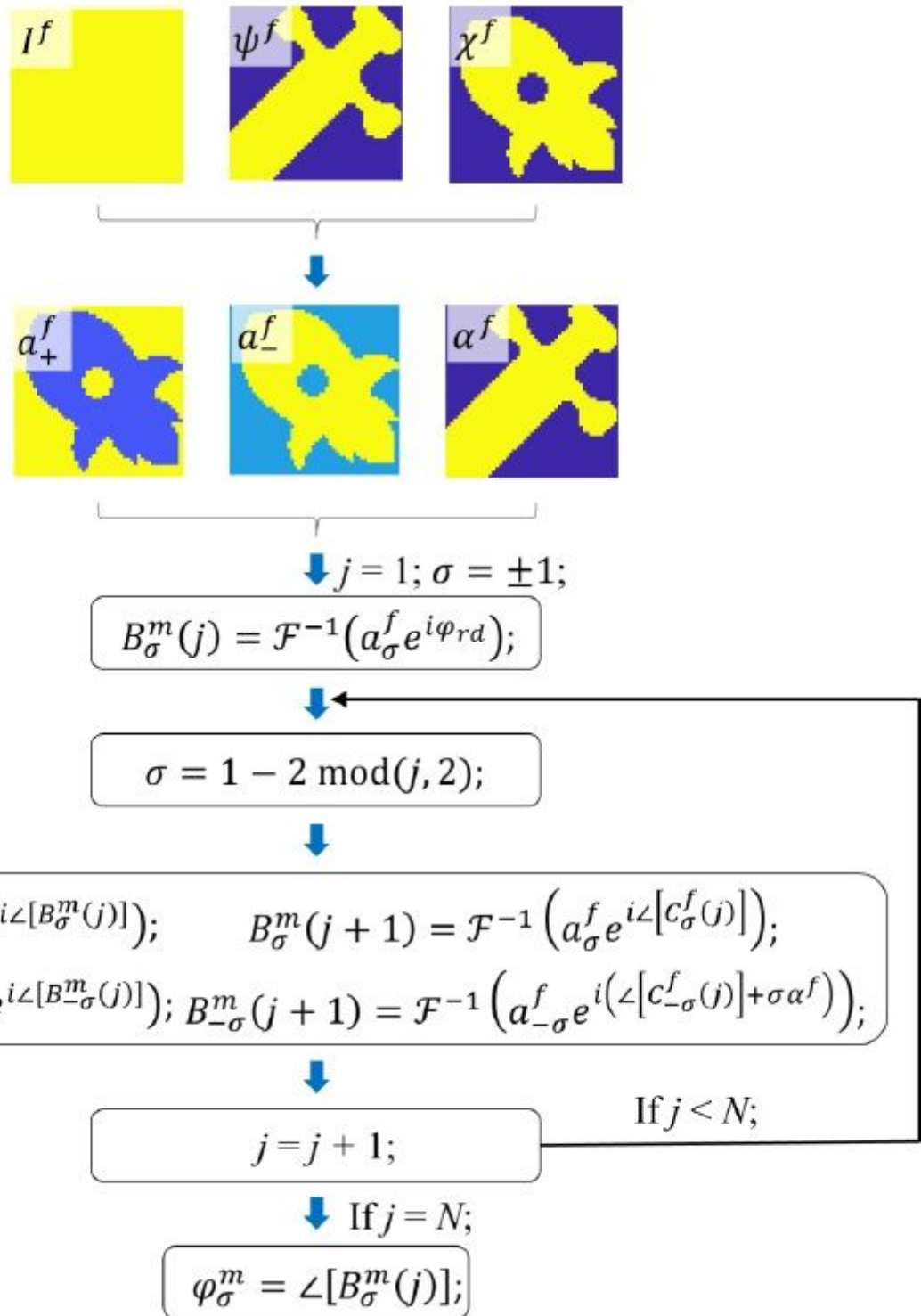


Figure 2

Modified iterative Fourier transform algorithm. With respect to intensity-only iterative Fourier transform algorithm, the current version considers several input information to realize diffraction patterns with arbitrary intensity, azimuth and ellipticity angles of the polarization. The algorithm converges to a vectorial profile optimizing the amplitude of both LCP (\boxplus) and RCP (\boxminus), and the phase difference between the two CP beams (\boxtimes). The notation \boxtimes represents the handedness of the CP beam, where + or +1 represents LCP and - or -1 represents RCP. A random phase of \boxtimes is used for the starting phase. The

number of iterations is $N = 100$. The final holographic phase of the metasurface is φ_{\pm} . The superscript m indicates the metasurface plane, f is the image plane in the far field. (See more details in Supplementary Note 1)

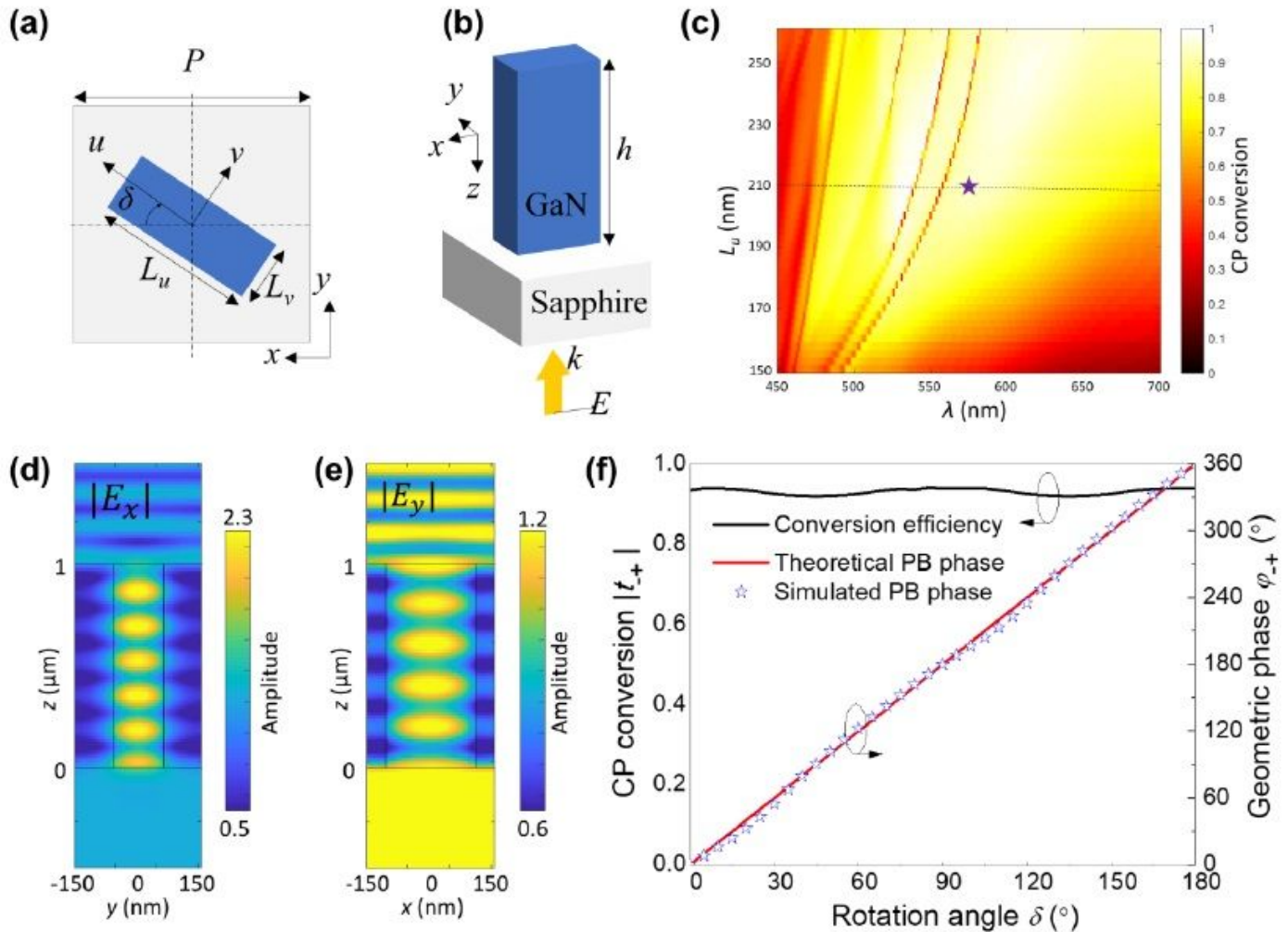


Figure 3

Simulated results of metasurface with birefringent GaN nanopillars on sapphire substrate with dimension of $P = 300$ nm and $h = 1$ μm . (a) Top view and (b) perspective view of one meta-structure. The numerical calculation is performed on unit cell of GaN nanopillar on sapphire substrate considering periodic boundary conditions on x and y . The width of the GaN nanopillar is fixed as $L_v = 120$ nm. (c) The simulated CP conversion by sweeping the length of the GaN nanopillar L_u from 150 nm to 260 nm in the wavelength range from 450 nm to 700 nm with zero rotation angle. The dash line represents the length of $L_u = 210$ nm. The purple star represents the wavelength at $\lambda = 575$ nm, which is the chosen point in d-f. (d) The simulated electric field distribution E_x at the plane of $x = 0$ and (e) E_y at the plane of $y = 0$. (f) By rotating the GaN nanopillars with an angle of δ from 0 to 180 $^\circ$, a near unity CP conversion is shown in the black curve and a geometric phase from 0 to 360 $^\circ$ is obtained. The simulated results are represented by the blue star, in 366 very good agreement with the expected PB phase calculation (red curve).

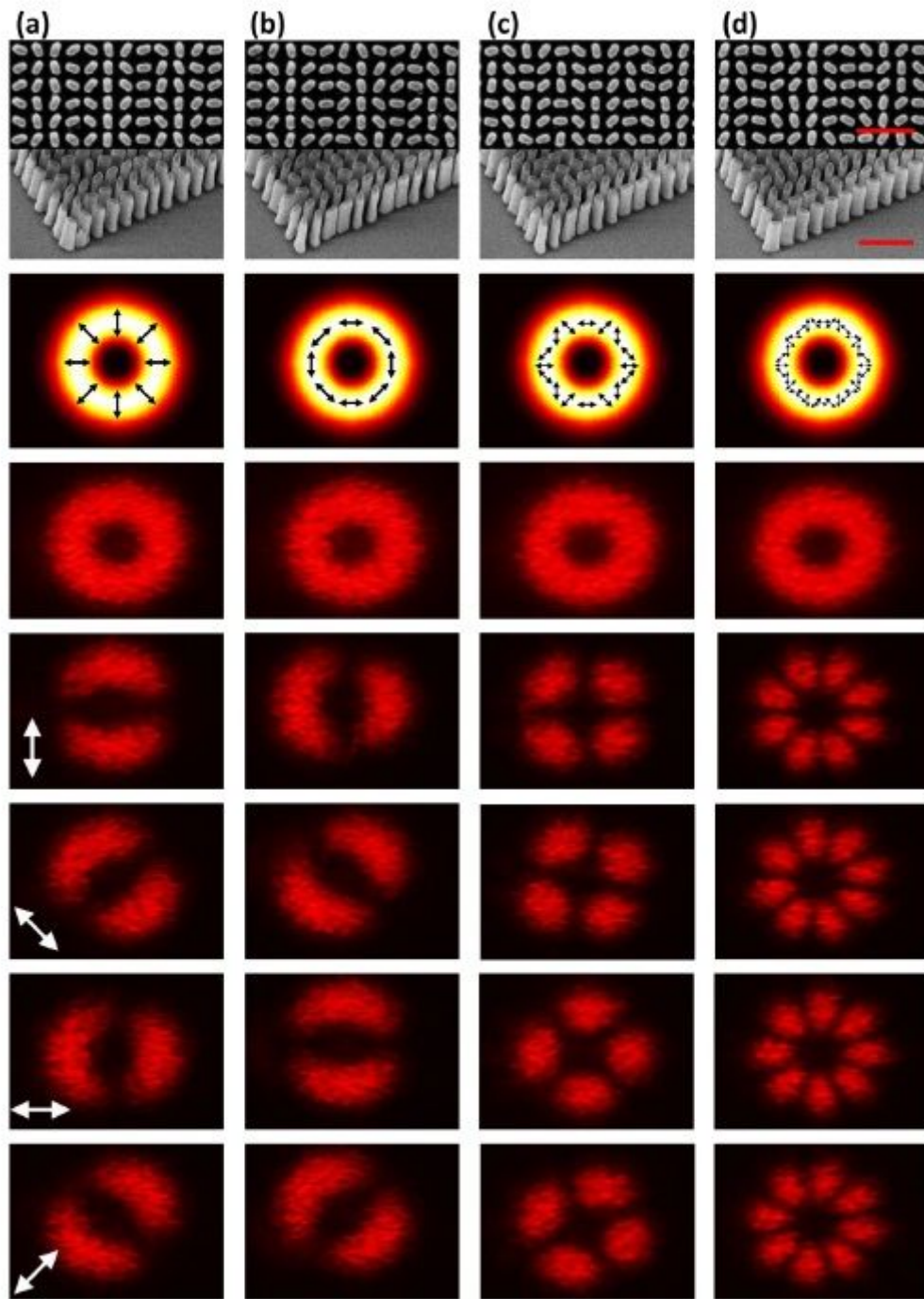


Figure 4

Fabricated results and optical measurement of the Stokes Polarization parameters of the donut polarization distributed field profile. Field distribution with (a) $l = 1, m = 0$, (b) $l = 1, m = 1$, (c) $l = -2, m = 0$, (d) $l = -4, m = 0$. Top row: fabricated results with the top view (top panels) and tilt view (bottom panels). The red scale bar represents $1 \mu\text{m}$. Second row: Intensity profiles of the designed vectorial fields. The black arrow represents the local polarization. Third row: measured intensity profiles of the field distributions without linear polarizer. Fourth to seventh rows: measured intensity profiles of the field

distributions with a linear polarizer. The white arrow represents the transmission axis of the linear polarizer.

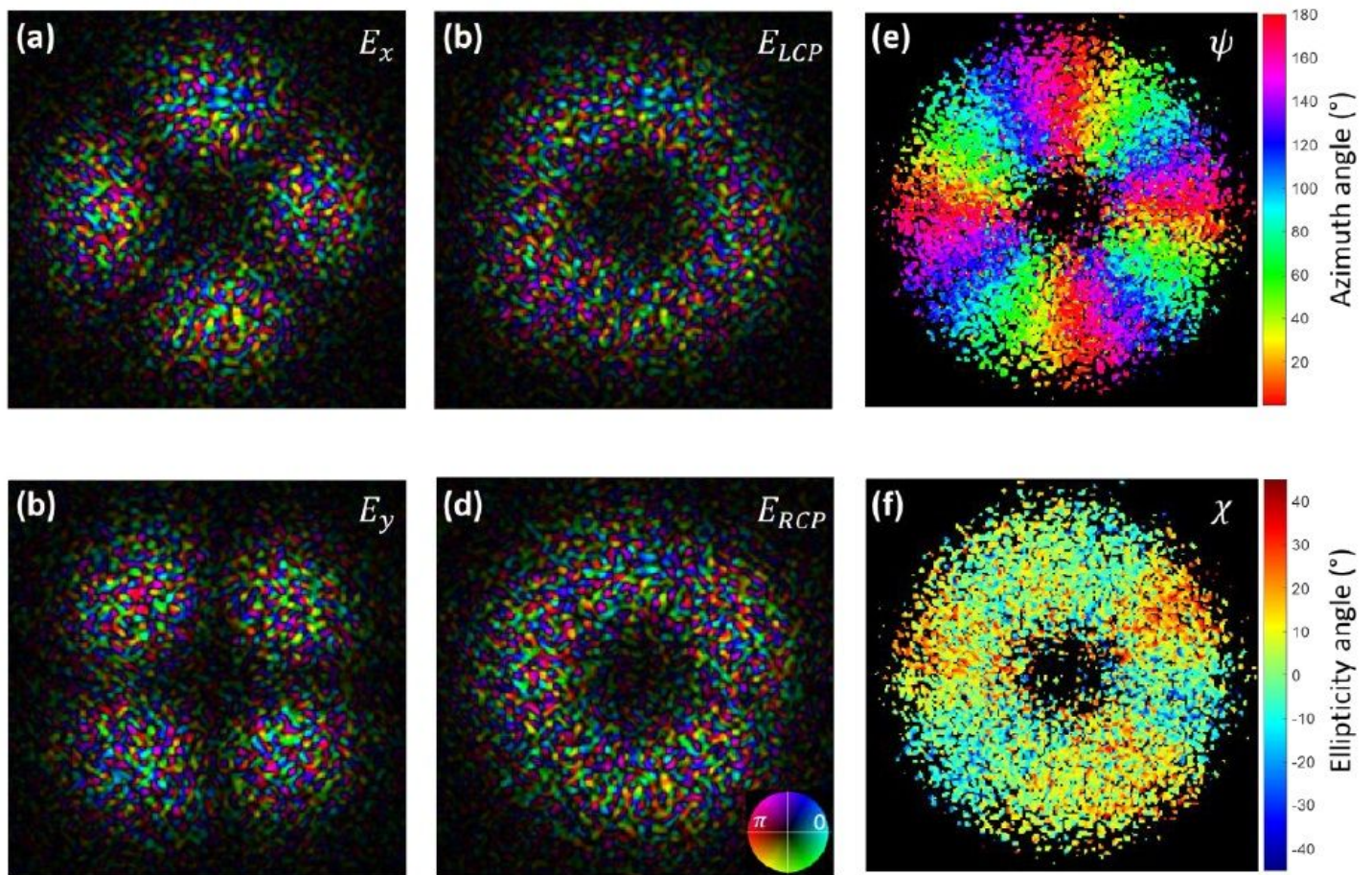


Figure 5

Complex amplitude and polarization information of far field as retrieved by the ptychographic measurement. Measured complex amplitude of (a) x-pol., (b) y-pol., (c) LCP and (d) RCP components. The phase profiles for the four polarization components show typical speckle phase distributions. The inset figure in (d) is the color bar with phase encoded as hue and amplitude as brightness. Measured (e) azimuth angle and (f) ellipticity angle of polarization information.

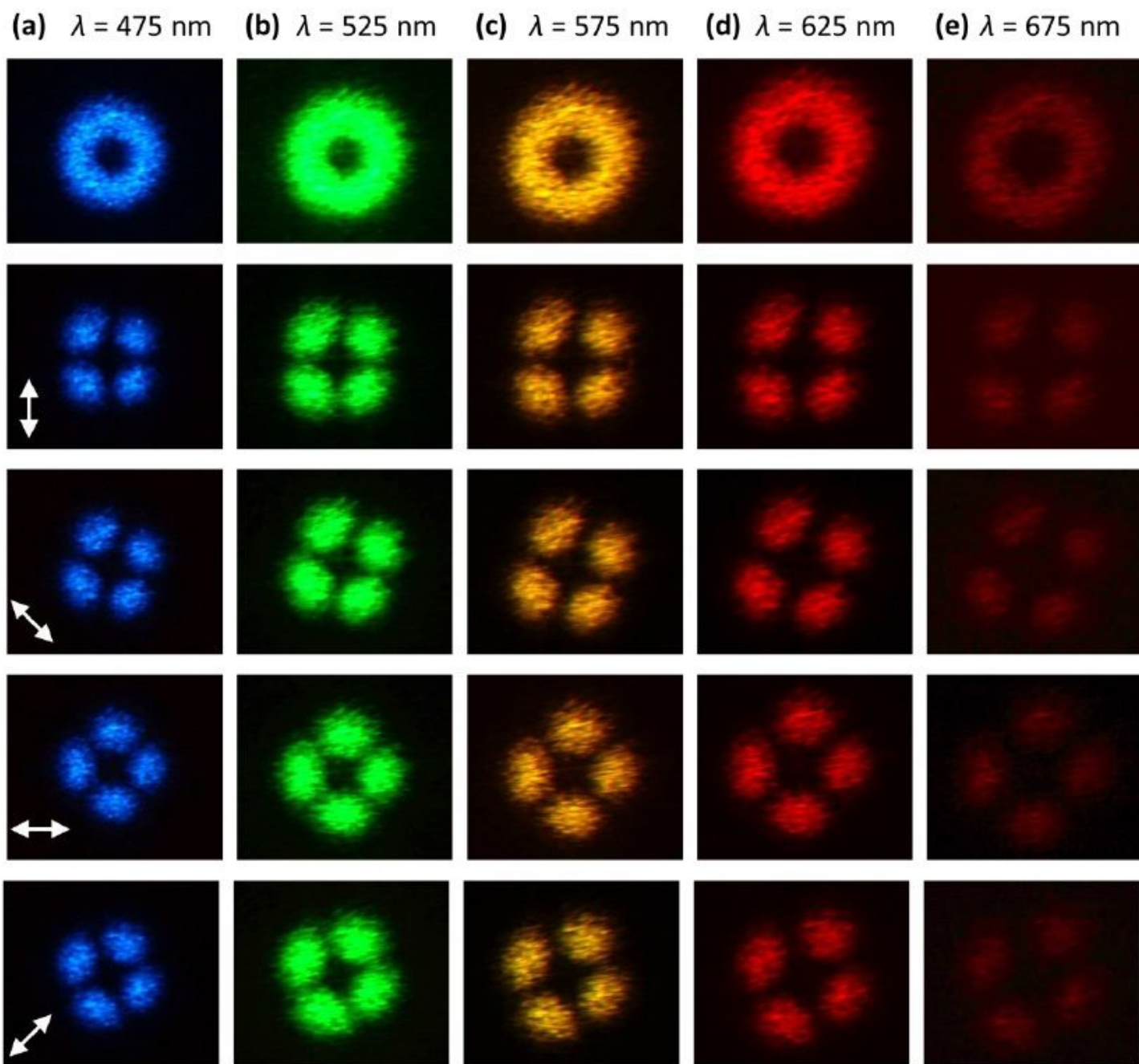


Figure 6

Broadband characterization of the vectorial metasurfaces designed for a field profiles with $l = -2$, $m = 0$. The measured intensity profiles at different wavelengths of (a) $\lambda = 475$ nm, (b) $\lambda = 525$ nm, (c) $\lambda = 575$ nm, (d) $\lambda = 625$ nm, (e) $\lambda = 675$ nm. Top row: measured intensity profiles without linear polarizer. Second to fifth rows: measured intensity profiles with a linear polarizer. The white arrow represents the transmission axis of the linear polarizer.

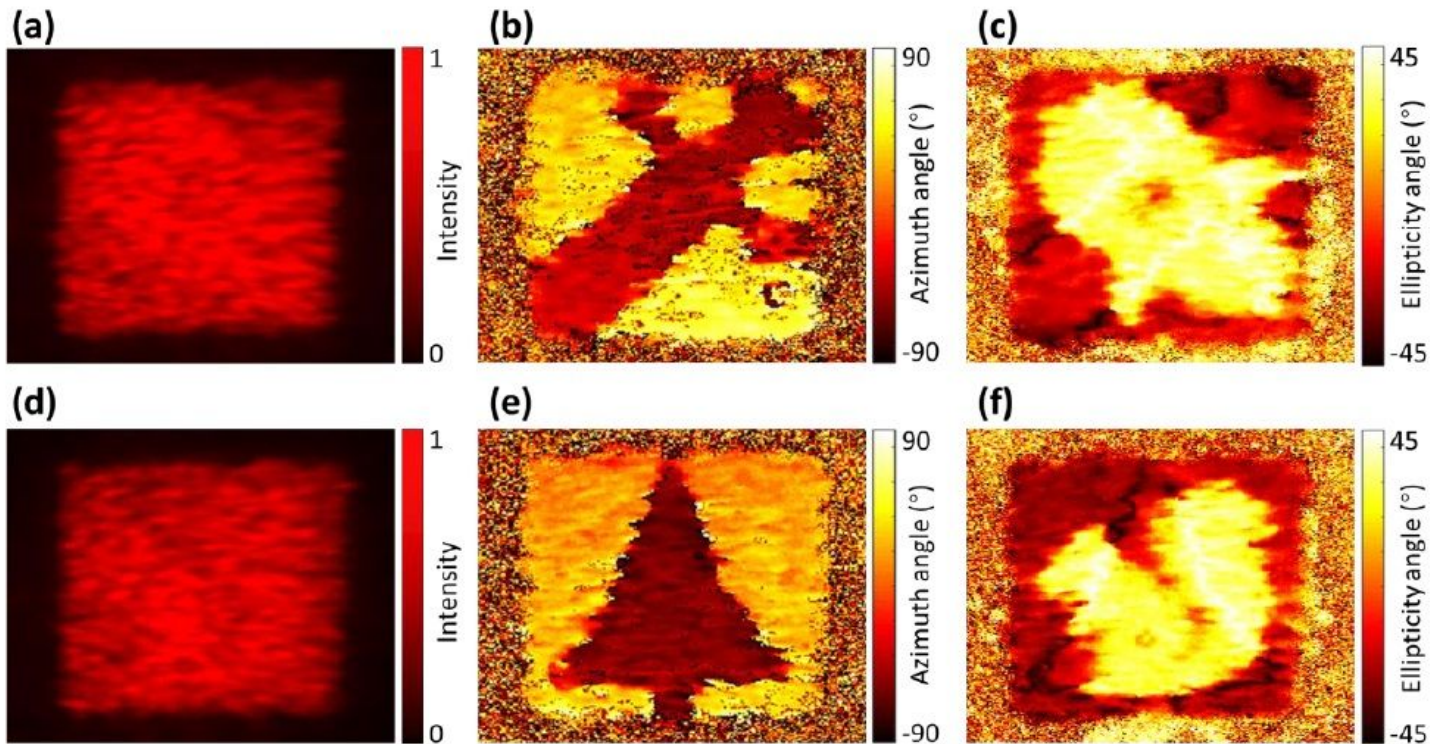


Figure 7

Measurement results of vectorial encoded images. (a)-(c) show the data obtained for the first metasurface design. (d)-(f) correspond to the data for the second metasurface design. (a)-(f) Measurement results using conventional optical setup to image the Stokes parameters. (a) and (d) Measured intensity, (b) and (e) azimuth angle, (c) and (f) ellipticity angle of the polarization. Both interfaces encode a similar uniformly distributed intensity profile as shown in (a) and (d). Color coded images displaying the ellipticity and the orientation, images reveal a “Blade”, a “Rocket”, a “Tree” and a “Squirrel” encoded polarization images as shown in (b), (c), (e) and (f).

Supplementary Files

This is a list of supplementary files associated with this preprint. Click to download.

- [NCSupplementary.pdf](#)
- [video01CVbeam.mp4](#)
- [video02BladeandRocket.mp4](#)
- [video03TreeandSquirrel.mp4](#)